Time-resolved Raman and luminescence spectroscopy of synthetic REE-doped hydroxylapatites and natural apatites

Amaury Fau, Olivier Beyssac, Michel Gauthier, Gérard Panczer, Olivier Gasnault, Pierre-Yves Meslin, Sylvain Bernard, Sylvestre Maurice, Olivier Forni, Jean-Claude Boulliard, et al.

Time-resolved Raman and luminescence spectroscopy of synthetic REE-doped hydroxylapatites and natural apatites

Fau A.[(1)], Beyssac O.[(1), *], Gauthier M.[(1)], Panczer G.[(2)], Meslin P.Y.[(3)], Bernard S.[(1)], Gasnault O.[(3)], Maurice S.[(3)], Forni O.[(3)], Boulliard J.C.[(1)], Bosc F.[(4)] and Drouet C.[(4)]

(1) IMPMC, UMR 7590 CNRS - Sorbonne Université - MNHN, Campus Jussieu, Case Courrier 115, 4 place Jussieu, F-75005 Paris (2) ILM, UMR5306 - UCBL – CNRS, 10 rue Ada Byron, F-69622 Villeurbanne (3) IRAP, UMR 5277 CNRS - Université Paul Sabatier Toulouse - CNES, 9 Avenue du Colonel Roche, F-31400 Toulouse (4) CIRIMAT, UMR 5085 CNRS - Université Paul Sabatier Toulouse - INP Toulouse, 4 allée Emile Monso F-31030 Toulouse

** Corresponding author : Olivier.Beyssac@upmc.fr*

Abstract

Apatites are phosphate minerals of broad interest in Earth and planetary sciences, and beyond. Using continuous and time-resolved spectroscopy, we investigate the Raman and luminescence signal from synthetic hydroxylapatites doped with trivalent Rare-Earth Elements (REE) dysprosium (Dy^{3+}), Europium (Eu^{3+}), Neodymium (Nd^{3+}) and Samarium (Sm^{3+}), as well as from natural apatites, with laser excitation at 532 nm and 785 nm. We demonstrate that time-resolved spectroscopy is extremely efficient to reject luminescence from Raman spectra or, alternatively, to investigate the luminescence signal without the interference of the Raman contribution. Time-resolved luminescence spectroscopy is found powerful to generate specific high-quality luminescence spectra for the REE emission activators in apatites by using appropriate combinations of delay and gate width for the time synchronization of the laser pulse and ICCD detector. This allows unambiguous detection and identification of the activators by avoiding overlapping of various emission signals in the luminescence spectra, which is particularly useful in the case of natural samples that often include several activators for luminescence. In the case of synthetic REE-doped apatites, a quenching process of luminescence due to the activator concentration is evidenced for Eu^{3+} and Sm^{3+}: the higher the concentration, the shorter the luminescence decay time. The interpretation of luminescence decay time in natural apatites is promising but more complex because of energy transfers between the various luminescence activators present in the mineral structure. Luminescence is a powerful signal to detect the presence of REE in apatites down to ppm levels, yet it is challenging to quantify the concentration.

Word counts ***, 11 figures, 2 tables

For submission to American Mineralogist (or European Journal Of Mineralogy)

Introduction

The calcium phosphate apatites with general formula [$Ca_5(PO_4)_3(F,Cl,OH)$] are among the most common accessory minerals in terrestrial rocks and in meteorites; they have also recently been identified *in situ* on Mars by the ChemCam LIBS instrument onboard the Curiosity rover (Forni et al. 2020). They are also a very important biomineral constitutive of bones or teeth as well as a primary source of phosphorous, a key element for life and many human activities. In Earth and planetary sciences, apatites are sensitive tracers of volatiles and fluid-rock interactions in terrestrial metamorphic rocks (Harlov 2015), terrestrial magmatic and volcanic rocks (Webster & Piccoli 2015) as well as in meteorites (McCubbin & Jones 2015). They are important minerals for thermochronological and geochronological investigations of processes occuring at various depths and temperatures (Chew & Spikings 2015). Last but not least, apatites offer an unusual range of applications and use for human activity making them a technological gem: this includes ecology, agronomy, biology, medicine, archeology, environmental remediation, and materials science (Rakovan & Pasteris 2015; Gomez-Morales et al. 2013). It is thereby important to constantly improve the tools for the characterization of the structure and chemistry of apatites. To this aim, vibrational spectroscopies like infrared and Raman, as well as luminescence spectroscopy provide rich information, and a number of practical advantages making them nowadays inevitable when exploring the physico-chemical properties of such minerals.

Raman spectroscopy is useful for a quick, non-destructive and non-ambiguous identification of apatites down to the microscale (Antonakos et al. 2007). In addition, Raman spectroscopy provides valuable information on the presence of OH^- in the halogen site and, more generally, on the type of apatite: hydroxyl- versus fluor- versus chlor- apatites (Antonakos et al. 2007). It can also be used to assess the cristallinity of apatite and to track possible carbonate incorporation in bioapatite through CO_3^{2-} substitution for PO_4^{3-} tetrahedra (Awonusi et al. 2007, and see Pasteris & Beyssac 2020 and references therein). Laser excitation during Raman analysis may also induce emission of luminescence in apatite. Luminescence is used here as a generic term describing all kinds of photoluminescence whatever the mechanism of light emission, e.g., fluorescence, luminescence, or phosphorescence (see Gaft et al. 2015 and Waychunas 2014 for further details). Because the luminescence signal can be extremely strong and can completely overwhelm the Raman signal, it is often considered as a severe limitation for proper Raman analysis. In some cases, the luminescence peaks can be so sharp that they actually may be confused with Raman peaks (Lenz et al. 2015). However, in many cases,

luminescence carries a rich and valuable information complementary to Raman (Gaft et al. 2015; Nasdala et al. 2004; Panczer et al. 2012; Waychunas 2014), particularly in apatites (Waychunas 2002; Gaft & Panczer 2013). Recent developments in Raman mapping further allow for mapping luminescence patterns in minerals at the microscale opening new avenues for the non-destructive investigation of internal microtexture of minerals (Nasdala et al. 2012; Lenz and Nasdala 2015).

One possibility to avoid or limit luminescence is to change the wavelength of the laser excitation used for Raman analysis in the range from the deep ultra-violet (UV) to the near infrared (IR). This approach works well in some cases but it is also limited by severe analytical challenges (e.g. deep UV) or by the poor Raman efficiency at high wavelength in the near IR region (Dubessy 2012; Beyssac 2020 for a review). Another possibility is to use time-resolved (TR) spectroscopy, which uses the different lifetimes of the Raman and luminescence processes. The Raman effect is actually a prompt phenomenon with an extremely short lifetime ($\approx 10^{-15}$ s). By contrast, the lifetime of luminescence processes in minerals is longer, ranging from fractions of nanoseconds to seconds and even more (Panczer et al. 2012; Gaft et al. 2015). By perfectly synchronizing in the time-domain a pulsed-laser (in the nanosecond range) with a gated intensified CCD (ICCD), it is possible to excite effectively the Raman effect and to reject efficiently most of the luminescence especially if it has a long decay time. Furthermore, time-resolved spectroscopy makes possible the exploration of the time decay or lifetime of luminescence, which is a measure of the transition probability between two specific levels. Such lifetime is then a specific and unique property of the luminescence signal (Gaft and Panczer 2013) for a given electronic transition in a precise crystallographic environnement.

Rare-Earth Elements (REE) also named lanthanides, are a large and very important group of elements in mineralogy and geochemistry. REE can actually be incorporated during mineral formation and evolution as trace elements in various mineral matrices. REE incorporation in minerals and further exchanges are fundamental in geochemistry and have provided key information on many geological processes. Optical properties like luminescence of REE as trace elements in minerals may be treated similarly to those of impurities in crystals. Since they behave as emission centers, here called luminescence activators, in minerals, their luminescence properties are used to track them by photoluminescence or to map them to detect possible internal zoning in minerals using cathodoluminescence (Waychunas 2014; Gaft et al. 2015) or photoluminescence (Lenz and Nasdala 2015). Because the apatite structure can accommodate a large variety of elements, it is a well adapted matrix for trapping minor and trace elements, in particular REE. In natural apatites, monitoring REE contents may then inform

on the constitution and evolution of local mineralogical grounds. On fossil bones, REE are progressively incorporated in bone apatite during diagenesis, upon enrichment from the surrounding minerals (Suarez et al., 2010). In the field of nanomedicine, the intentional incorporation of luminescent REE as dopants in synthetic apatites allows nanoparticle tracking in medical diagnosis (Mondéjar et al., 2007, Al-Kattan et al., 2014); and their luminescence signal has been recently exploited, coupled to Raman and histology analyses, to follow the skin penetration of apatite-based colloidal nanoparticles for dermatological applications (Choimet et al. 2020). Luminescence spectroscopy is thus a powerful technique to investigate REE in such mineral compounds, however it is still largely under-exploited.

Simple yet valuable investigations of luminescence properties in minerals can be done with a conventionnal Raman spectrometer, an instrument largely accessible nowadays in laboratories, and even for field studies (Jehlicka et al. 2017). Notably, there are more and more combined LIBS and Raman investigations often with a single instrument (see Fau et al. 2019 and references therein): LIBS provides chemistry and Raman provides mineralogy. LIBS can detect major and many trace elements but is not able to detect REE at low concentration. Luminescence spectroscopy could fill the gap and provide detection of REE for such studies. This is particularly the case for the SuperCam instrument, which is an instrumental suite to be deployed on Mars onboard the NASA Perseverance rover in 2021. SuperCam will combine remote LIBS and time-resolved Raman and luminescence spectroscopy, and could benefit from the detection of REE by luminescence for a better understanding of geochemical processes at the surface of Mars (Wiens et al. 2021, Maurice et al. in press, Beyssac 2020).

The purpose of the present study is to investigate (i) the structure by Raman spectroscopy and (ii) the luminescence properties, of synthetic REE-doped apatites used as standards as well as natural apatite specimens. In the case of synthetic hydroxylapatites, they are doped with one single trivalent lanthanide (Eu^{3+}, Sm^{3+}, Nd^{3+} or Dy^{3+}) at relevant geological concentration and we explore the corresponding luminescence spectra. We also document the decay time of the luminescence signal for various concentrations of the doping REE element. The case of natural apatites is interesting but more complex to interpret since several emission centers for luminescence are present within a given sample. Comparison of the time-resolved luminescence spectra of synthetic and natural apatites is first discussed for a better interpretation of the peaks in the emission spectra of luminescence. In addition, we discuss possible factors affecting the luminescence signal of REE in apatites, in particular those controling the evolution of luminescence in the time domain like quenching and/or sensitizing phenomena.

Apatite: an overview on Raman and luminescence

Apart from few exceptions, such as pure chlorapatite (monoclinic system, space group $P2_1/b$), apatites most generally crystallize in a hexagonal structure in the $P6_3/m$ space group symmetry. These compounds contain five crystallographic sites: the Ca1 (9-fold coordination) and Ca2 (7-fold coordination) sites, the P site, the halogen/OH^- site and "defect" sites following the terminology by Waychunas (2002). More details on the topology of these sites and, more generally, on the crystal structure of apatites may be found in Hughes and Rakovan (2002) or Hughes and Rakovan (2015).

The Raman spectrum of apatites has been extensively described by O'Shea et al. (1974) and Antonakos et al. (2007). Interestingly, apatites include the PO_4^{3-} and OH^- ions that can be easily detected by Raman (Rey et al. 2014). The most intense peak, often used for a quick detection of phosphate minerals is located at ≈ 960 cm^{-1} for apatites and is due to the ν_1 symmetric stretching mode of PO_4^{3-}. Additionnal peaks due to PO_4^{3-} are the doubly degenerate ν_2 bending mode at ≈ 430 cm^{-1}, the triply degenerate antisymmetric ν_3 stretching mode at ≈ 1060 cm^{-1} and the triply degenerate ν_4 bending mode at ≈ 580 cm^{-1}. OH^-, when present, contributes a large band at ≈ 3570 cm^{-1} while F^- and Cl^- are not directly detected by Raman. However, the presence of F^- and/or Cl^- in the OH^- site may induce a shift of the various PO_4^{3-} vibration modes as well as modifications in the OH^- domain due to a modified configuration of hydrogen bonds.

Luminescence of apatites has been extensively studied from a long time (Blasse 1975). Waychunas (2002) and Gaft et al. (2015) made comprehensive reviews while other studies were dedicated to the specific luminescence of Eu (Kottaisamy et al. 1994; Gaft et al. 1997), or more generally to the REE luminescence patterns in apatites (Reisfeld et al. 1996; Czaja et al. 2010). Some studies are dedicated to other emission centers such as U^{6+} and $(UO_2)^{2+}$ (Panczer et al. 1998) or Mn^{2+} (Gaft et al. 2015) in apatite. Waychunas (2002) provided a detailed description of the type of luminescence activators and described the link with the apatite structure. The five sites of apatites can be occupied by activators, but the most common ones, *i.e.* those observed in natural apatites, in particular REE or Mn^{2+}, actually go in the Ca1 and Ca2 sites (Waychunas 2002).

One important point to emphasize is that some activators like Mn^{2+} will generate very broad emission bands because of the different symmetries of the ground and excited electronic states. Alternatively, activators for which the change in configurational coordinate between

ground and excited state is small, or even null, will generate very narrow emission lines. This is the case for REE^{3+}, for which (i) the parity forbidden *4f-4f* transitions should be weak unless being enhanced by symmetry crystal fields establishing a relationship between intensity and site symmetry, and (ii) the allowed *4f-5d* transitions generally lead to slightly broader bands. Activators generally do not behave independently in the apatite structure and some may transfer part or all of their energy to other nearby activators becoming sensitizers. This applies to some REE^{3+} that can be sensitized by Mn^{2+}: this triggers and enhances emission by REE^{3+} and decreases that of Mn^{2+} (Marfunin 1979). Conversely, some authors have argued that Eu^{2+} can act as a sensitizer of Mn^{2+} luminescence (Knutson et al. 1985; Kottaisamy et al. 1994). Of course, not only a single but many REE are generally present in natural apatites making very likely the occurrence of transitions with similar energy. This may favor not only single energy transfer but also multiple ones involving several REE (Waychunas 2002).

In natural apatites, REE can easily substitute for Ca and become emission centers for luminescence in the crystallographic structure of the host apatite. Most REE can be incorporated in either the Ca1 or Ca2 sites and be luminescent as trivalent or divalent ions. When trivalent REE ions are incorporated in substitution of Ca^{2+}, this is necessarily associated to a charge balance mechanism (Hosseini et al., 2014), thus generating other "abnormalities" or defects in the apatitic lattice which may somewhat alter locally the site symmetry (which may have an impact on luminescence features). Studies by steady-state luminescence, *i.e.* continuous excitation in the time domain, in general using UV excitation, have demonstrated that natural apatite luminescence is dominated by divalent Mn^{2+} and Eu^{2+} and trivalent Ce^{3+}, Dy^{3+}, Nd^{3+} and Sm^{3+} (Gaft et al. 2001). The particular case of Eu in apatites has been extensively studied by Gaft et al. (1997, 2001) and Kottaisamy et al. (1994). These studies give an overview of the complexity of REE luminescence in apatites but also of the rich information that can be extracted with this technique. In apatite, Eu^{2+} luminescence appears as a single band at ≈ 450 nm due to a 4*f*-5*d* transition with a lifetime of 500 ns (Gaft et al. 2001). It has been assigned to the Ca2 sites by Kottaisamy et al. (1994). Eu^{3+} luminescence is characterized by lines at 590, 617, 651 and 695 nm and was assigned to the Ca1 site (Gaft et al. 2001). In synthetic Eu-doped apatites under specific excitation, additional lines were observed at 575, 628 and 712 nm and were assigned to Eu^{3+} in the Ca2 site (Morozov et al. 1970).

Samples: synthetic and natural apatites

REE-doped synthetic hydroxylapatites

The REE-doped hydroxylapatites were synthesized at CIRIMAT Toulouse at relevant geological concentrations, following the method described by Hosseini et al. (2014). The REE selected for this study are trivalent Eu^{3+}, Sm^{3+}, Nd^{3+} and Dy^{3+} because they are important geochemical tracers and their luminescence patterns in apatite is known. We selected trivalent REE because they emit luminescence in spectral windows relevant to our instrumental setups and they are also observed in natural samples. The REE salts used were purchased from SIGMA-ALDRICH. First, we prepared a stock solution of each REE doping element with a concentration of 0.04 mol/L by dissolving respectively europium(III) chloride hexahydrate, ($EuCl_3.6H_2O$ – molecular weight MW: 366.41 g/mol), samarium(III) nitrate hexahydrate, ($Sm(NO_3)_3\ 6H_2O$ - MW: 444.47 g/mol), dysprosium(III) chloride hexahydrate, ($DyCl_3.6H_2O$ - MW: 376.95 g/mol) and neodymium(III) nitrate hexahydrate, ($Nd(NO_3)_3.6H_2O$ - MW: 438.35 g/mol) in deionized water. Preparation of hydroxylapatites was based on coprecipitation obtained by mixing two starting solutions: solution A contained calcium nitrate tetrahydrate ($Ca(NO_3)_2.4H2O$ - MW: 236.15 g/mol) dissolved in deionized water to obtain a calcium concentration of 0.4 mol/L, and solution B contained di-ammonium hydrogenphosphate ($(NH_4)_2.HPO_4$ - MW: 132.06 g/mol) dissolved in deionized water at a phosphate concentration of 0.13 mol/L. REE-doped hydroxylapatites at desired concentrations of doping element were finally obtained by mixing solutions A and B and the relevant REE stock solution diluted as necessary and to which 2 mL of 30% NH_4OH ammonia were added to increase the pH of the solution in order to facilitate the hydroxylapatite precipitation. The obtained mixtures are then placed in an oven at 143 °C for a duration of 14 hours. Three successive washing stages with deionized water and centrifugation for 3 minutes at 7500 rpm were carried out in order to remove traces of ammonia and unreacted salts present in the precipitating medium. Finally, the samples were dried in an oven at 80 °C for a minimum of 8 hours.

Natural apatites

The natural apatite samples were selected from the collection de Minéraux (Sorbonne Université, Paris) as raw millimetric to centimetric samples. Table 1 summarizes the main information for each apatite specimen studied. These samples are either single crystals or polycrystalline aggregates.

Methodology: analytical techniques

Chemical analyses

Major and trace element analyses for natural and synthetic apatites were done by alkali fusion of rock samples ($LiBO_2$), followed by concentration measurements using an ICP-OES Icap 6500 (Thermoscientific) for major elements, and an ICP-MS X7 (Thermoscientific) for trace elements (protocol by Carignan et al., 2001). Analyses were performed at the Service d'Analyse des Roches et Minéraux (SARM, CNRS, Nancy, France). For Dy^{3+}-doped synthetic apatites, chemical analysis was performed on only one sample as the luminescence signal was not detected for these samples (see below). Table 1 and Table 2 present the major (oxide wt%) and trace element (mg/g) composition of the natural and synthetic REE doped samples respectively. Figure 1 depicts the chondrite normalized REE patterns for the natural apatites.

X-ray diffraction

XRD was used to verify the apatitic nature of the synthetic apatites prepared. We used a Panalytical Pro MPD operating at 40 kV, 40 mA with Co-Kα radiation wavelength of λ = 1.788965 Å. Diffractograms were recorded from 5 to 90° in a 2θ scale and 0.033° step size during 3 cycles of 1.5 hour.

Infrared spectroscopy

Fourier transform infrared (FTIR) was used to characterize and verify the cristallinity and molecular structure of the synthetic apatites. We used a Nicolet Magna 560 working under dry air. All measurements were done in transmission mode with a Globar / Nernst lamp source and a DTGS-CsI detector. Spectra were obtained in the 4000-400 cm^{-1} range with a resolution of 2 cm^{-1} and by averaging 200 spectra. Before analyses, samples were prepared by mixing 1 mg of REE-doped hydroxylapatite with 300 mg of dried KBr.

Continuous-wave Raman spectroscopy

All samples were analyzed using a continuous-wave (CW) Raman microspectrometer Renishaw InVia Reflex for point analyses and Raman hyperspectral mapping when needed. Measurements were performed using a green 532 nm solid-state laser focused on the sample through a Leica DM2500 microscope with a long-working distance 50X objective (NA = 0.55). This configuration yields a planar resolution of ≈1-2 µm for a laser power delivered at the sample surface set at less than 1 mW using neutral density filters to prevent irreversible thermal damages. This corresponds to a laser irradiance in the range of 0.3-1.3 10^9 $W.m^{-2}$. All measurements were performed with a circularly polarized laser using a ¼-wave plate placed before the microscope in order to minimize polarization effects. The Raman signal was

dispersed by a grating with 2400 lines/mm and the signal was analyzed with a RENCAM CCD detector. Some samples (Nd^{3+}-doped hydroxylapatites) were also analyzed using a 785 nm diode laser yielding a spot size of a few μm^2 for excitation and a 1200 lines/mm grating for dispersion, the rest of the setup being the same.

For Raman mapping and the acquisition of hyperspectral maps, the sample was moved with an appropriate step size using a XYZ Renishaw motorized stage. Laser focus was optimized by correcting topographic variation prior to analysis (surface mode using the Renishaw Wire 4.3 software) and all maps were processed using the Wire 4.3 software. More about Raman mapping can be found in Bernard et al. (2008). All measurements were performed at room temperature and spectra were recorded directly on the raw samples without any preparation.

Note that CW Raman spectroscopy also provides steady-state luminescence emission spectra in the range 532-720 nm with excitation at 532 nm, or in the range 785-930 nm with excitation at 785 nm.

Time-resolved Raman and luminescence spectroscopy

All samples were also analyzed using a custom-built time-resolved Raman and luminescence spectrometer described by Fau et al. (2019). The laser is a nanosecond (1.2 ns FWHM, 1 mJ per pulse) pulsed diode-pumped solid-state (DPSS) laser operating at 532 nm with a 10 to 2000 Hz repetition rate. The laser is slightly defocused at the sample surface through a microscope objective (MPlan Apo Mitutoyo 20X, NA= 0.42) and the Raman and luminescence signals are collected in the backscattering geometry. In addition, the laser is circularly polarized thanks to a ¼-wave plate placed before the microscope in order to minimize polarization effects. In this setup, a Notch filter cuts off the Rayleigh scattering at ≈ 90 cm^{-1} and the signal is collected by an optical fiber and sent into a modified Czerny-Turner spectrometer (Princeton Instruments IsoPlane 320) coupled with an intensified Princeton Instruments PIMAX4 ICCD camera. The fine control of both time delay and gating time of the camera allows sub-nanosecond time resolution experiments thanks to a precise synchronization between the laser pulse and the ICCD. This spectrometer has three motorized gratings which can be selected depending on the spectral window and resolution requested for the experiment. Irradiance associated with a pulsed laser can be estimated as $Q/(\tau S)$, with $Q = P/f$ being the laser energy per pulse, P being the time-integrated laser power measured at the surface of the sample, f the laser repetition rate, τ the pulse duration, and S the surface of the laser spot on the sample. For these experiments, irradiance was set at $\approx 10^{10}$ $W.m^{-2}$ which is conservative even in the case of absorbing minerals (Fau et al. 2019).

Time-resolved Raman and luminescence spectroscopy: overview

The luminescence signal is generally much stronger than the extremely weak Raman signal. One way to separate the Raman signal from luminescence is to exploit the fact that these two processes have very different lifetimes using time-resolved spectroscopy. Lifetime corresponds to the time spent in any excited state, e.g. vibrationnal for Raman or electronic for luminescence, before it returns to the ground state. For luminescent compounds, de-excitation is expected to occur by the emission of a photon. However, depending on the energy gap between the excited and ground states of a given luminescent center (e.g. Eu^{3+} or Tb^{3+} ions), de-excitation may partially also occur by a non-radiative process as in the form of vibrational energy (phonon) if a good energetic correspondence is found, as was reported in apatites with O-H vibrations (Al-Kattan et al., 2014). However, even in this case, luminescent signals remain strong. In all cases, light absorption is "immediate" in the range of 10^{-18} seconds, while Raman and emission of luminescence are longer processes. Relaxation from virtual vibrational levels is typically in the range of 10^{-15} seconds for Raman and can be considered as "immediate" at our experimental time scale. On the other hand, going back from excited electronic levels to the ground state is much slower, and the lifetime of luminescence covers a wide time range from the nanosecond (e.g., organic fluorescence, Lakowicz 2006) to milliseconds or even seconds (e.g., Cr^{3+} or REE^{3+} in minerals, Gaft et al. 2015).

Time-resolved spectroscopy uses a pulsed excitation signal synchronized with a gated detector. The main idea is that the Raman signal will last only during the excitation pulse, while the luminescence will be excited within the pulse but will continue to emit and decay after the pulse. Using a short time gate perfectly synchronized with the laser pulse and matching it in the time domain allows rejection of most of the luminescence signal and maximization of the collection of the Raman signal. Time-resolved spectroscopy further allows the collection of only the luminescence signal without any Raman contribution by simply opening the detector gate just after the laser pulse. The Raman signal is then completely vanished and is absent in the spectrum while luminescence is still present. In this study, we investigate the emission spectra: all spectra were obtained with an incident excitation laser at 532 nm, or 785 nm in the sole case of Nd^{3+} using the CW spectrometer. Such excitation wavelengths are likely not optimal for triggering absorption and thereby emission of luminescence. Going towards UV would be more efficient, but these wavelentgths constitute a good compromise for combining Raman and luminescence investigations.

The custom-built time-resolved instrument used for this study offers an excellent synchronization making possible the exploration of luminescence with various lifetimes. To this aim, an appropriate combination of delays (moment the detector gate opens with respect to the laser pulse) and gate width has to be used.

Lastly, this technique allows proper characterization of the time decay of luminescence by doing time sweep experiments: a post-pulse detector gate with appropriate opening duration is shifted at various time delays, and the integrated intensity of the signal can be plotted versus the shift time (delay). These data allow calculating the lifetime and give further information on the nature of the electronic transition and, more practically, on the identification of the emission center (Lakowicz 2006; Gaft & Panczer 2013; Gaft et al. 2015).

Luminescence decay is given by

$$I(t) = I_0 e^{-\frac{t-t_0}{\tau}} \qquad \text{equation (1)}$$

with I_0 the number of photons emitted at time t_0, τ the lifetime of the considered transition. The analysis of luminescence decay is done by measuring the number of photons received during a time period controled by the gate width and by shifting this gate through time after the laser pulse. Critical parameters are then the gate width t_g and t_s the time increment by which the gate is shifted.

Using the time-resolved setup one effectively measures:

$$F(T) = \int_T^{T+t_g} I_0 e^{-\frac{t-t_0}{\tau}} dt \qquad \text{equation (2)}$$

in n+1 points given by

$$T_k = t_0 + k\, t_s \qquad \text{equation (3)}$$

After normalisation by the gate width and introduction of equation (3), F(T) becomes

$$F(T_k) = I_0 t_g e^{-\frac{kt_s}{\tau}} \left(\frac{1-e^{-\frac{t_g}{\tau}}}{\frac{t_g}{\tau}} \right) \qquad \text{equation (4)}$$

Several aspects about methodological information can be retrieved from this equation. First, the gate width does not influence the experimental evaluation of τ because, whatever τ, $\left(\frac{1-e^{-\frac{t_g}{\tau}}}{\frac{t_g}{\tau}} \right)$ is a constant value even if $\frac{t_g}{\tau}$ is large. For a reliable assesment of τ, luminescence must have decayed notably so that $\frac{kt_s}{\tau} > \frac{1}{4}$. To have an acceptable uncertainty, the statistics has to be good so *k* value has to be large. Lastly, the unpredictable factor is the intensity of luminescence. The lower the intensity, the larger the accumulation of signal required to obtain a correct spectrum. This is an important parameter to consider in such experiments, which has

an important effect on the duration of the time decay experimental analysis (time sweep experiment).

To exploit efficiently the luminescence spectra and time sweep experiments, a specific script was written using Python. A Voigt function is used for fitting all the peaks and includes a Gaussian component with a fixed FWHM value at 13 cm^{-1} corresponding to the instrument resolution and a Lorentzian component due to the luminescence signal. A linear baseline defined by two points automatically calculated as the lowest points from a predefined region in the spectrum is subsracted prior to luminescence peak fitting, and no normalization is performed before data processing. For each time sweep experiment, the selected peaks are fitted on the first spectrum of each series, when the signal-to-noise ratio is high, by letting free the Lorentzian FWHM as well as the area and position of the Voigt band. A second series of fit is then performed on the whole series of spectra with just the Voigt band area as a free parameter. Lifetime is determined from the semi-logarithmic representation of intensity versus time delay and is taken as the slope of the regression line extracted from the experimental points.

In addition, time-resolved spectroscopy allows exciting selectively luminescence emissions from various emission centers if they have different lifetime decays. This is very promising as one challenge in the interpretation of luminescence spectra, especially in the case of natural minerals like apatites, is precisely that emission peaks from various emission centers often overlap in the spectral domain.

Results and discussion

Physico-chemical characterisation of the REE-doped synthetic apatites

XRD diffractograms of synthetic hydroxylapatites display all the main characteristic peaks of hydroxylapatite thus confirming the apatitic nature and the good crystallinity of the samples produced (Figure 2). These finding are corroborated by FTIR spectroscopy analyses (Figure 3). All the infrared spectra obtained are very similar among the different samples with various concentrations of the doping element and exhibit the characteristic spectral features of hydroxylapatite (Rey et al., 2014). The presence of an OH^- peak at 3570 cm^{-1} (O-H stretching) and an associated libration band at 632 cm^{-1} confirm that the synthesis yielded hydroxylated apatites. The presence of trace impurities in the form of nitrate NO_3^- ions is detectable as a minor contribution (≈1383 cm^{-1}), and hydration of the synthetic apatites is detectable via a wide band due to the vibration of H_2O molecules around 3400 cm^{-1}.

Chemical data for major and trace elements obtained on the synthetic apatites are presented in Table 1. Table 1 shows that the range of concentrations obtained is wide for Eu^{3+}, Sm^{3+} and Nd^{3+} from tens to thousands of ppm, while Dy^{3+} was properly incorporated into the analyzed synthetic apatite as well (although the luminescence signal is not detected, see below). We also note that some samples have been slightly contaminated by the presence of another lanthanide than the one used for synthesis. This is likely due to the unperfect purity level of the initial REE salts. For instance, the sample of hydroxylapatite doped with a concentration of 24 ppm of samarium also has a europium concentration of around 5 ppm. Continuous-wave Raman mapping was performed on some synthetic hydroxylapatites to assess their homogenity by obtaining thousands of spectra on a given sample. These maps showed that the structure of these samples is homogeneous because the FWHM and peak position of the main ν_1 peak is rather constant with only minor variations (<1 cm^{-1}).

Time-resolution: a considerable improvement for Raman spectroscopy

Figure 4 depicts representative CW micro-Raman spectra obtained at random positions on the synthetic apatites. Depending on the REE doping element, the Raman peaks characteristic of apatite are clearly visible (Dy^{3+}), more or less visible (Sm^{3+}) or not visible (Eu^{3+}). Note that the case of Nd^{3+} is different: Raman peaks are clearly visible when excited at 532 nm but non-visible with excitation at 785 nm because the luminescence of Nd^{3+} is extremely strong in the near IR region. Indeed, the Raman signal remains constant in Raman shift for all the synthetic samples, while emission of luminescence after light absorption strongly depends on the excitation wavelength for each REE. Eu^{3+} ions are highly excited at 532 nm and luminescence completely masks the Raman signal while for Sm^{3+} luminescence is less strong and the Raman signal is visible. In the case of Dy^{3+}-doped apatites, 532 nm is out of the range of absorption (excitation) and emission of luminescence is not observed while Raman bands are nicely recorded.

Alternatively, Figure 5 shows a representative Raman spectrum obtained with the time-resolved Raman instrument with a short gate (5 ns) centered on the laser pulse. This spectrum was obtained with a highly luminescent hydoxylapatite doped with 23,936 ppm Sm^{3+}, but similar spectra were obtained with all other synthetic doped hydroxylapatites. The difference is striking with CW Raman spectroscopy as no luminescence bands are detected while all the Raman peaks are clearly visible, including the OH^- bands. This is due to the efficient rejection of the REE luminescence which has a long lifetime for the REE considered here.

The case of the natural apatites is more complex when analyzed with CW Raman spectroscopy (Figure 6): a very strong background including some peaks due to Raman and luminescence is observed in all spectra. In general, only the main ν_1 symmetric stretching mode of PO_4^{3-} is observed in these spectra (e.g., samples Tyrol, Saxe and Renfrew) while the other modes are hardly detected in some samples (Slyudyanka and Imilchil). Clearly, using Time-resolved Raman spectroscopy makes possible the rejection of almost all the luminescence contributions in these natural apatites and the recording of high-quality Raman spectra without any luminescence interference. It is particularly interesting in the case of REE because they generate intense and thin peaks that can be easily confused with Raman peaks in phosphate minerals but also in other mineral phases like zircon as discussed by Lenz et al. (2015).

In the REE-doped synthetic hydroxylapatites, the Raman shift of the ν_1 symmetric stretching mode of PO_4^{3-} is nearly constant at about 960 ± 1 cm^{-1}. In the natural apatites, this PO_4^{3-} mode is in the range 963.8 to 965.4 cm^{-1}. A strong OH^- band is observed in all the synthetic apatites while it is not observed in the natural apatites, even in the time-resolved Raman spectra. The Raman shift of the ν_1 symmetric stretching mode of PO_4^{3-} is actually sensitive to the nature of the apatite (Ashley et al. 2018): it occurs at ≈ 960 cm^{-1} in pure hydroxylapatite, ≈ 961 cm^{-1} in pure chlorapatite and ≈ 965 cm^{-1} in pure fluorapatite. This is due to the fact that Cl^- has a much larger ionic radius compared to F^-. From these observations, Raman investigations confirm that the synthetic apatites are pure hydroxylapatites as assessed from infrared and XRD characterization. The natural apatites are solid solutions in between the three endmembers (OH^--Cl^--F^- apatites) and the Raman spectra do not show a notable contribution of OH^-, hence the contribution of the hydroxylapatite endmember is minor in these samples. Based on the Raman shift of the ν_1 symmetric stretching mode of PO_4^{3-}, most natural samples appear to have Raman shift values corresponding to high levels of F^- in the halogen site and these samples likely correspond essentially to fluorapatites. Only the case of the Imilchil sample is slightly different with a lower shift and this sample has likely a higher Cl^- level in the halogen site.

Time-resolved luminescence: detecting REE and other emission centers

If time-resolved spectroscopy allows to get rid of luminescence features in Raman spectra, it is also powerful to eliminate the Raman contribution from the luminescence spectra, and thereby to unambigously study the luminescence signal. For this, the ICCD gate just has to be opened

after the laser pulse when the Raman signal is completely relaxed and is no longer active. For many minerals including apatites, the main luminescence emission lines can be attributed rather confidently unless there is a strong overlap between various luminescence signals making the interpretation complex (Gaft et al. 2015).

In the natural apatites, the total Raman and luminescence spectra obtained in continuous-wave (CW) illumination are actually not staightforward to interpret (Figure 6). This is due to the multiple emission lines of the various REE incorporated in the mineral structure in addition to the contribution of other activators like Mn^{2+}. Mn^{2+} is actually likely partly responsible for the broad background observed in most of these samples. Figures 7 illustrates the capability of time-resolved spectroscopy to separate the Raman and luminescence signals in the Durango apatite. In addition, this technique allows further investigating luminescence by generating spectra specific of activators with various lifetimes by selecting appropriate combinations of delays and gates. In the case of the Durango sample (Figure 7), this technique allows to retrieve a clear spectrum of the short-lifetime luminescence signal from erbium by opening a short gate (1,500 ns) just after the laser pulse (delay 6 ns). Erbium luminescence is otherwise completely covered by longer lifetime emissions in the continuous wave emission spectrum. In a complementary approach, this technique allows to analyze just the contribution of long lifetime emissions by opening a wide gate (450,000 ns) long after the laser pulse (delay 1,500 ns). Ideally, if activators are expected in a given sample as well as the approximative lifetime of their emission is known, appropriate combinations of delay and gate should allow maximization of the emission signal for each activator. This makes time-resolved spectroscopy an extremely powerful tool to avoid overlapping of various luminescence contributions from REE and other emission centers in apatites and other mineral phases.

Alternatively, at a constant delay (e.g. just after the laser pulse) one can open the gate with increasing values from 10 to thousands of ns (here we limit at 450,000 ns just before the next laser pulse arriving at 500,000 ns at 2 KHz) to test the detection of various emission centers with different lifetimes. This is illustrated on Figure 8 for the Durango apatite. With short gates (<1,000 ns), only the short lifetime emission signal, here Er^{3+}, is visible in the spectrum because of the less efficient rejection for short lifetime luminescence. Increasing the gate width allows for the detection of other peaks corresponding to longer lifetime emission signals from Sm^{3+}, Eu^{3+} and Dy^{3+}. This approach is useful to obtain neat emission spectra for short lifetime emissions but also to assess the rejection efficiency of the instrumental time resolution.

Luminescence spectra retrieved from the synthetic REE-doped hydroxylapatites are easier to interpret (Figure 4). In the case of Eu^{3+}, a strong luminescence signal is observed at

all concentrations including the lowest. This signal is composed by several bands with two main massifs centered at 590 and 620 nm corresponding respectively at $^5D_0$-$^7F_1$ et $^5D_0$-$^7F_2$ transitions. Other less important peaks are observed at ≈ 655 nm and ≈ 570-580 nm and correspond to $^5D_0$-$^7F_3$ et $^5D_0$-$^7F_0$ transitions. The case of Sm^{3+} is very similar to Eu^{3+} with two main massifs occurring at ≈ 600 and 650 nm. Dy^{3+} has no emission bands observed in any of the spectra even at concentrations as high as 500 ppm. It contrasts with the natural apatites in which Dy^{3+} emission bands were observed at ≈ 590 nm. One possible explanation is that emission by Dy^{3+} is sensitized either by another REE and/or by Mn^{2+} in the natural samples. Marfunin (1979) and Waychunas (2002) have actually reported that Mn^{2+} can act as a sensitizer for the luminescence of some REE: Mn^{2+} absorbs incident energy and transfers it to REE which then emit light. In the case of the synthetic REE apatite, Dy^{3+} is alone and not excited therefore it does not emit luminescence. In the case of Nd^{3+}, the luminescence peaks are detected only with a continuous instrument with excitation at 785 nm because it correponds to the best excitation and the emitted signal occurs in the near infrared part of the spectrum. This sample could not be studied with the time-resolved instrument (excitation at 532 nm). The Nd^{3+} emission is characterized by an intense, broad massif with several peaks in the range 850 to 925 nm.

Deconvolution of luminescence spectra: a challenging task

A simple visual inspection of the spectra shows that (i) luminescence spectroscopy is extremely sensitive down to the ppm level and (ii) the overall intensity of the luminescence signal dramatically increases with the activator concentration. Figure 9 depicts the total intensity (sum of areas for all peaks after peak fitting) of the luminescence signal for the massifs centered at 620 nm and 600 nm as a function of Eu^{3+} and Sm^{3+} concentration respectively. For figure 9, the luminescence signal was analyzed with continuous spectroscopy and time-resolved spectroscopy at laser repetition rate of 100 Hz: excitation/collection is continuous in the former case while the latter case corresponds to the signal mostly generated by a single laser pulse (the signal has almost completely decayed between two pulses). There is a sharp increase of the intensity incresing concentration: the higher is the concentration, the stronger is the luminesce signal. However, it is difficult to retrieve any quantitative information from this observation as the absolute intensity of the signal depends on many other parameters like the sample surface state and grain size, the sample effective optical absorption or the sample orientation with respect to the incident laser beam.

Using the developed Python script, the Eu^{3+} and Sm^{3+} spectra of synthetic hydroxylapatites at different concentrations and different delays from time sweep experiments were deconvoluted. For Eu^{3+}, the fit was performed on the massif centered at 620 nm with 8 bands while it was done on the massif centered at 600 nm for Sm^{3+} with 5 bands. This is a rather challenging task as these massifs are likely generated by a much larger number of electronic transitions. For instance, Sm^{3+} luminescence in apatite results from a large number of f-f electronic transitions. The $4f^5$ configuration of Sm^{3+} ion has at least 73 multiplets yielding 198 energy levels via spin-orbit interactions (Axe et Dieke, 1962). Not all these transitions are excited and not all of them will generate emission if excited. The number of bands selected may appear somewhat arbitrary, however it is determined by what is actually observed in the spectra. First, in both the Eu^{3+} and Sm^{3+} cases, it was observed that within the considered massif, all the peaks decay with the same lifetime. Second, to investigate the effect of the activator concentration, several plots of the various peaks FWHM or relative intensities were made. In general, no significant trends were observed except an increase of the 597 nm/604 nm peak area ratio in the case of Sm^{3+}.

One purpose of these investigations was to check for possible correlations between any spectral parameter and the luminescence activator concentration. This would provide a proxy for quantification or semi-quantification of the activator thanks to its luminescence signal. No such correlation was found for the spectral parameters. This contrasts with the Cr^{3+} luminescence in ruby glasses. Cr^{3+} luminescence in ruby has been extensively studied and results from optical absorption into the $^4T_2$ and $^2T_2$ levels and the two well-known emission bands R1 (at 694.25 nm at 300K) and R2 (at 692.74 nm at 300K) originate from the ^2E level (see Syassen 2008 and references therein). Chervin et al (2001) studied the spectral parameters of emission spectra of ruby glasses spheres doped at various concentrations of Cr^{3+} as pressure gauge for optically transparent high-pressure cells. They established clear correlations between the Cr^{3+} concentration and the FWHM of both the R1 and R2 emission lines at various excitation energies: the higher the concentration, the broader the two lines. Such correlations can be used as a first-order proxy for Cr^{3+} concentration in ruby glasses.

In the case of natural apatites, the situation is even more challenging due to the multiple overlapping luminescence signals detected in these samples. If time-resolved spectroscopy can be powerful to discriminate short versus long lifetime signals in the emission spectra, one challenge is that many overlapping REE emission signals have similar lifetimes among them and with other emission signals (e.g. from Mn^{2+}) making a challenge any deconvolution of the spectra.

572

573 ***Luminescence lifetime: a powerful yet complex physical parameter to interpret***

574

575 Time sweep experiments were performed on the natural and synthetic apatites to investigate the
576 lifetime of Eu^{3+} and Sm^{3+} emission. For this, the laser repetition rate was set at 200 Hz, and 20
577 spectra with a gate of 1 ms were taken with the first being recorded 200 µs after the laser pulse
578 and the delay being augmented by 200 µs for each successive spectrum with a final spectrum
579 at 4 ms after the pulse. The total intensities of the 8 peaks composing the massif at 620 nm for
580 Eu^{3+} and of the 5 peaks of the massif at 600 nm for Sm^{3+} are plotted against time (here the
581 delay) as represented in figure 10. For both Eu^{3+} and Sm^{3+}, the higher the concentration of the
582 activator, the faster the decay of luminescence. From figure 10, the luminescence lifetime for
583 each decay curve for Eu^{3+} and Sm^{3+} can be calculated from equation (4) and plotted against the
584 activator concentration as shown on Figure 11. In both cases, there is a clear correlation between
585 the luminescence lifetime and the activator concentration, even at low concentration: the higher
586 the concentration, the shorter the luminescence lifetime. Such an acceleration of the decay of
587 the luminescence signal by increasing the concentration of the activator may be a consequence
588 of a concentration quenching effect. By increasing the number of activators in the mineral
589 structure, some activators may directly transfer their excitation energy to a neighbour activator
590 through a non-radiative process, *e.g.* by a vibrationnal process. Such a correlation has already
591 been observed for other materials like Gd_2O_3:Eu^{3+} nanocrystals (Meza et al. 2014). These
592 authors established a clear correlation between the lifetime and Eu^{3+} concentration from
593 experimental data that they were able to model with a simple rate equation model. They
594 interpreted such correlation as the consequence of a concentration quenching involving energy
595 transfer among Eu^{3+} ions but also with O^{2-}. Also, as mentioned previously, in hydroxylated
596 apatites, part of the de-excitation energy may contribute to some O-H stretching, which was
597 evidenced in deuterated experiments (Al-Kattan et al., 2014).

598 Time sweep experiments were run with the natural apatites in the same configuration as
599 the one used for the synthetic samples. The Eu^{3+} massif at 620 nm and Sm^{3+} massif at 600 nm
600 were fitted following the procedure used previously in the case of the synthetic apatites. Time
601 decay figures can be generated for each natural apatite (not represented here) and the lifetime
602 of Eu^{3+} and Sm^{3+} emission signals can be calculated. Several spots were analyzed on each
603 natural apatite to have an insight into the intra-sample chemical and structural heterogeneity.
604 Figure 11 depicts all the calculated lifetimes for both natural and synthetic apatites for Eu^{3+} and
605 Sm^{3+} luminescence versus the concentration in Eu^{3+} and Sm^{3+} measured by ICP-MS. First of

606 all, natural samples show systematically a significant dispersion for the calculated lifetimes
607 compared to synthetic samples. Notably, in the case of Eu^{3+}, the concentrations observed in the
608 natural samples are lower than those of the synthetic ones. In addition, for Eu^{3+}, the scattering
609 of the lifetime values for natural samples covers a range almost similar to the complete range
610 of lifetime values in the synthetic samples. This dispersion may reflect first the intra-sample
611 chemical zoning for REE which is often observed in natural apatite minerals. More generally,
612 there is no clear correlation between the lifetime and the activator concentration for the natural
613 samples and the points retrieved from natural samples do not fall on the correlation observed
614 with the synthetic samples. They are generally above the curve obtained from the synthetic
615 samples, which means that luminescence is generally longer to relax in natural samples
616 compared to synthetic ones.
617 A major difference between natural and synthetic samples is the presence in the former
618 of several REE activators and even sometimes of other activators like Mn^{2+}, while the synthetic
619 samples are doped with a single activator (apart minor impurities mentioned above). There is
620 no easy interpretation for the different behavior but there is likely a complex interplay between
621 the various activators in the natural samples involving sensitizing and/or quenching processes
622 for luminescence among REE and/or with other activators. For instance, using time-resolved
623 spectroscopy, Czaja et al. (2010) demonstrated the effective energy transfer between
624 praseodymium Pr^{3+} and samarium Sm^{3+} in natural apatites and showed its effect on the lifetime
625 of emission luminescence of these crystals. Such effects are absent in the synthetic samples
626 which are doped with a single REE activator.
627 As already mentionned by Gaft and Panczer (2013), it is important to distinguish a
628 theoretical “true” decay time or lifetime from a real effective decay time or lifetime. The true
629 lifetime is an intrinsic physical parameter of a given transition for an activator in a crystal
630 structure in the absence of any non-radiative processes and obtained under precise conditions
631 (e.g. temperature, pressure). The effective lifetime is the one measured in the laboratory that
632 can be close to the true one in the case of “perfect” samples with one single activator and no
633 other impurities. But it can be very different in the case of natural samples. The effective
634 lifetime is actually possibly influenced primarily by external parameters like temperature or
635 analytical parameters, orientation of the crystal with respect to the polarization of the incident
636 laser beam; also irradiance may play a role for instance. Overall, as shown by this study, it can
637 depend on the internal properties of the samples like the presence of other impurities (other
638 activators, defects), which may trigger complex sensitizing and/or quenching phenomenons by
639 energy transfer.

Implications

Time-resolved spectroscopy is a very powerful tool to combine Raman and luminescence spectroscopy as it allows performing both, separately and without interference in the spectral data. In the case of REE, time-resolved spectroscopy is extremely efficient to detect and identify them in accessory mineral phases like apatites or other phosphate minerals, titanite or zircons. Owing to its capability to scan the time domain and selectively analyze each emission signal, time-resolved spectroscopy provides information that is not accessible to steady-state, *i.e.* continuous-wave, spectroscopy. A major achievement would be to reach some quantification, or at least semi-quantification of luminescence activators in mineral phases from the luminescence signal, either directly from the spectra or through the study of lifetime. This may be possible in the case of systems involving one single activator such like Cr^{3+} in natural or synthetic ruby, or in our synthetic REE-doped hydroxylapatites. It is a complex challenge in systems involving more than one activator as activators are likely to transfer energy among themselves generating complex quenching and/or sensitizing interactions and complexifying the interpretation of the time-resolved data.

In a close future, on Mars, the Mars2020 SuperCam time-resolved instrument onboard the Perseverance rover should benefit from time-resolved Ramand and luminescence spectroscopy for detecting and investigating REE not only martian phosphates but more generally inmartian rocks opening new avenues for our understanding of geochemical processes at work on this planet (Wiens et al. 2021; Maurice et al. 2021).

References

Al-Kattan, A., Santran, V., Dufour, P., Dexpert-Ghys, J., and Drouet, C. (2014) Novel contributions on luminescent apatite-based colloids intended for medical imaging. *Journal of Biomaterials Applications*, 28, 697-707. https://doi.org/10.1177/0885328212473510

Antonakos, A., Liarokapis, E., Leventouri, T. (2007) Micro-Raman and FTIR studies of synthetic and natural apatites. *Biomaterials* 28, 3043–3054. https://doi.org/10.1016/j.biomaterials.2007.02.028

Ashley, K.T., McKeeby, B.E., Harlov, D.E., Bodnar, R.J., Ramsey, M.S. (2018) High-Resolution Raman Spectroscopy Constraints on Apatite Halogen Composition: Implications for Planetary Volcanism and Igneous Processes. Abstract for the Lunar and Planetary Science Conference 1483.

Awonusi, A., Morris, M.D., Tecklenburg, M.M.J. (2007) Carbonate Assignment and Calibration in the Raman Spectrum of Apatite. *Calcified Tissue International* 81, 46–52. https://doi.org/10.1007/s00223-007-9034-0

Axe, J.D., Dieke, G.H. (1962) Calculation of Crystal‐Field Splittings of Sm^{3+} and Dy^{3+} Levels in LaCl3 with Inclusion of J Mixing. *Journal of Chemical Physics* 37, 2364–2371. https://doi.org/10.1063/1.1733011

Bernard, S., Beyssac, O., Benzerara, K. (2008) Raman Mapping Using Advanced Line-Scanning Systems: Geological Applications. *Applied Spectroscopy* 62, 1180–1188. https://doi.org/10.1366/000370208786401581

Beyssac, O. (2020) New trends in Raman spectroscopy: from high-resolution geochemistry to planetary exploration. *Elements* 16, 117-122. https://doi.org/10.2138/gselements.16.2.117

Blasse, G. (1975) Influence of local charge compensation on site occupation and luminescence of apatites. *Journal of Solid State Chemistry* 14, 181–184. https://doi.org/10.1016/0022-4596(75)90009-2

Carignan J, Hild P, Mevelle G, Morel J, Yeghicheyan D (2001) Routine analyses of trace element in geological samples using flow injection and low pressure on-line liquid chromatography coupled to ICP-MS: a study of geochemical reference materials BR, DR-N, UB-N, AN-G and GH. Geostandards Newsletter, 25, 187-198. doi:10.1111/j.1751-908X.2001.tb00595.x

Chervin, J.C., Canny, B., Mancinelli, M. (2001) Ruby-spheres as pressure gauge for optically transparent high pressure cells. *High Pressure Research* 21, 305–314. https://doi.org/10.1080/08957950108202589

Choimet, M., Tourrette, A., Marsan, O., Rassu, G., Drouet, C. (2020) Bio-inspired apatite particles limit skin penetration of drugs for dermatology applications. *Acta Biomaterialia* 111, 418-428. https://doi.org/10.1016/j.actbio.2020.05.010

Chew, D.M., Spikings, R.A. (2015) Geochronology and Thermochronology Using Apatite: Time and Temperature, Lower Crust to Surface. *Elements* 11, 189–194. https://doi.org/10.2113/gselements.11.3.189

Czaja, M., Bodył, S., Lisiecki, R., Mazurak, Z. (2010) Luminescence properties of Pr^{3+} and Sm^{3+} ions in natural apatites. *Physics and Chemistry of Minerals* 37, 425–433. https://doi.org/10.1007/s00269-009-0344-9

Dubessy J, Caumon M-C, Rull F, Sharma S (2012) Instrumentation in Raman spectroscopy: Elementary theory and practice. In: Dubessy J, Caumon M-C, Rull F (eds) Raman Spectroscopy Applied to Earth Sciences and Cultural Heritage, European Mineralogical Union and Mineralogical Society of Great Britain & Ireland, London, pp 83-172

Fau, A., Beyssac, O., Gauthier, M., Meslin, P.Y., Cousin, A., Benzerara, K., Bernard, S., Boulliard, J.C., Gasnault, O., Forni, O., Wiens, R.C., Morand, M., Rosier, P., Garino, Y., Pont, S., Maurice, S. (2019) Pulsed laser-induced heating of mineral phases: Implications for laser-induced breakdown spectroscopy combined with Raman spectroscopy. *Spectrochimica Acta Part B: Atomic Spectroscopy* 160, 105687. https://doi.org/10.1016/j.sab.2019.105687

Forni, O., Meslin, P.-Y.,Drouet, C., Cousin, A., David, G., Mangold, N., Dehouck, E., Rampe, E.B., Gasnault, O., Beck, P., Nachon, M., Newsom, H., Blaney, D. L., Clegg, S. M., Ollila, A.M., Lasue, J., Maurice, S., and Wiens, R.C. (2020) Apatites in Gale Crater. Abstract for the Lunar and Planetary Sciences Conference, Houston, 2020.

Gaft, M., Panczer, G. (2013) Laser-induced time-resolved luminescence spectroscopy of minerals: a powerful tool for studying the nature of emission centres. Mineralogy and Petrology 107, 363–372. https://doi.org/10.1007/s00710-013-0293-3

Gaft, M., Panczer, G., Reisfeld, R., Uspensky, E. (2001) Laser-induced time-resolved luminescence as a tool for rare-earth element identification in minerals. *Physics and Chemistry of Minerals* 28, 347–363. https://doi.org/10.1007/s002690100163

Gaft, M., Reisfeld, R., Panczer, G. (2015) Modern Luminescence Spectroscopy of Minerals and Materials, 2nd ed, Springer Mineralogy. Springer International Publishing.

Gaft, M., Reisfeld, R., Panczer, G., Shoval, S., Champagnon, B., Boulon, G. (1997) Eu^{3+} luminescence in high-symmetry sites of natural apatite. Journal of Luminescence, *Luminescence and Optical Spectroscopy of Condensed Matter* 72–74, 572–574. https://doi.org/10.1016/S0022-2313(96)00229-3

Gomez-Morales, J., Iafisco, M., Delgado-Lopez, J.M., Sarda, S., and Drouet, C. (2013) Progress on the preparation of nanocrystalline apatites and surface characterization: Overview of fundamental and applied aspects. Progress in Crystal Growth and Characterization of Materials, 59, 1-46. https://doi.org/10.1016/j.pcrysgrow.2012.11.001

Harlov, D.E. (2015) Apatite: A Fingerprint for Metasomatic Processes. *Elements* 11, 171–176. https://doi.org/10.2113/gselements.11.3.171

Hosseini, S.M., Drouet, C., Al-Kattan, A., Navrotsky, A (2014) Energetics of lanthanide-doped calcium phosphate apatite. *American Mineralogist* 99, 2320–2327. https://doi.org/10.2138/am-2014-4930

Hughes, J.M., Rakovan, J. (2002) The Crystal Structure of Apatite, $Ca_5(PO_4)_3(F,OH,Cl)$. *Reviews in Mineralogy and Geochemistry* 48, 1–12. https://doi.org/10.2138/rmg.2002.48.1

Hughes, J.M., Rakovan, J.F. (2015) Structurally Robust, Chemically Diverse: Apatite and Apatite Supergroup Minerals. *Elements* 11, 165–170. https://doi.org/10.2113/gselements.11.3.165

Jehlička, J., Culka, A., Bersani, D., Vandenabeele, P. (2017) Comparison of seven portable Raman spectrometers: beryl as a case study. *Journal of Raman Spectroscopy* 48, 1289–1299. https://doi.org/10.1002/jrs.5214

Knutson, C., Peacor, D.R., Kelly, W.C. (1985) Luminescence, color and fission track zoning in apatite crystals of the Panasqueira tin-tungsten deposit, Beira-Baixa, Portugal. *American Mineralogist* 70, 829–837.

Kottaisamy, M., Jagannathan, R., Jeyagopal, P., Rao, R.P., Narayanan, R. (1994) Eu^{2+} luminescence in $M_5(PO_4)_3X$ apatites, where M is Ca^{2+}, Sr^{2+} and Ba^{2+}, and X is F^-, Cl^-, Br^- and OH^-. *Journal of Physics D: Applied Physics* 27, 2210–2215. https://doi.org/10.1088/0022-3727/27/10/034

Lakowicz, J.R. (2006) Plasmonics in Biology and Plasmon-Controlled Fluorescence. *Plasmonics* 1, 5–33. https://doi.org/10.1007/s11468-005-9002-3

Lenz, C., and Nasdala, L. (2015) A photoluminescence study of REE^{3+} emissions in radiation-damaged zircon. *American Mineralogist* 100, 1123–1133. https://doi.org/10.2138/am-2015-4894CCBYNCND

Lenz, C., Nasdala, L., Talla, D., Hauzenberger, C., Seitz, R., Kolitsch, U. (2015) Laser-induced REE^{3+} photoluminescence of selected accessory minerals — An "advantageous artefact" in Raman spectroscopy. *Chemical Geology* 415, 1–16. https://doi.org/10.1016/j.chemgeo.2015.09.001

Marfunin, A.S., 1979. Spectroscopy, Luminescence and Radiation Centers in Minerals. Springer Science & Business Media.

Maurice, S., Wiens, R.C., Bernardi, P. *et al.* (in press) The SuperCam Instrument suite on the Mars 2020 Rover: Science objectives and Mast-Unit Description. *Space Science Reviews.*

McCubbin, F.M., Jones, R.H. (2015) Extraterrestrial Apatite: Planetary Geochemistry to Astrobiology. *Elements* 11, 183–188. https://doi.org/10.2113/gselements.11.3.183

Meza, O., Villabona-Leal, E.G., Diaz-Torres, L.A., Desirena, H., Rodríguez-López, J.L., Pérez, E. (2014) Luminescence Concentration Quenching Mechanism in Gd2O3:Eu^{3+}. *The Journal of Physical Chemistry A* 118, 1390–1396. https://doi.org/10.1021/jp4119502

809 Mondéjar, S.P., Kovtun, A., Epple, M. (2007) Lanthanide-doped calcium phosphate
810 nanoparticles with internal chystallinity and with a shell of DNA as fluorescent probes in cell
811 experiments. *Journal of Materials Chemistry* 17, 4153-4159.
812 https://doi.org/10.1039/B708258D
813
814 Morozov, A.M., Morozova, L.G., Trofimov, A.K., Feofilov, P.P. (1970) Spectral and
815 luminescent characteristics of fluorapatite single crystals activated by rare-earth ions. *Optika i*
816 *Spektroskopiya* 29, 1106–1118.
817
818 Nasdala, L., Beyssac, O., William Schopf, J., Bleisteiner, B. (2012) Application of Raman-
819 based images in the Earth sciences, in: Zoubir, A. (Ed.), Raman Imaging: Techniques and
820 Applications, Springer Series in Optical Sciences. Springer Berlin Heidelberg, Berlin,
821 Heidelberg, pp. 145–187. https://doi.org/10.1007/978-3-642-28252-2_5
822
823 Nasdala, L., Smith, D.C., Kaindl, R., Ziemann, M.A. (2004) Raman spectroscopy: Analytical
824 perspectives in mineralogical research, in: Papp, G., Weiszburg, T.G., Beran, A., Libowitzky,
825 E. (Eds.), Spectroscopic Methods in Mineralogy. Mineralogical Society of Great Britain and
826 Ireland, Germany, pp. 281–343. https://doi.org/10.1180/EMU-notes.6.7
827
828 O'Shea, D.C., Bartlett, M.L., Young, R.A. (1974) Compositional analysis of apatites with
829 Laser-Raman spectroscopy: (OH,F,Cl)apatites. *Archives of Oral Biology* 19, 995–1006.
830 https://doi.org/10.1016/0003-9969(74)90086-7
831
832 Panczer, G., De Ligny, D., Mendoza, C., Gaft, M., Seydoux-Guillaume, A.-M., Wang, X.
833 (2012) Raman and fluorescence, in: Ferraris, G., Dubessy, J., Caumon, M.-C., Rull, F. (Eds.),
834 Raman Spectroscopy Applied to Earth Sciences and Cultural Heritage. European
835 Mineralogical Union, pp. 61–82. https://doi.org/10.1180/EMU-notes.12.2
836
837 Panczer, G., Gaft, M., Reisfeld, R., Shoval, S., Boulon, G., Champagnon, B. (1998)
838 Luminescence of uranium in natural apatites. *Journal of Alloys and Compounds* 275–277,
839 269–272. https://doi.org/10.1016/S0925-8388(98)00318-1
840
841 Pasteris, J.D., and Beyssac, O. (2020) Welcome to Raman Spectroscopy: Successes,
842 Challenges, and Pitfalls. *Elements* 16, 87-92. https://doi.org/10.2138/gselements.16.2.87
843
844 Rakovan, J.F., Pasteris, J.D. (2015) A Technological Gem: Materials, Medical, and
845 Environmental Mineralogy of Apatite. *Elements* 11, 195–200.
846 https://doi.org/10.2113/gselements.11.3.195
847
848 Reisfeld, R., Gaft, M., Boulon, G., Panczer, C., Jørgensen, C.K. (1996) Laser-induced
849 luminescence of rare-earth elements in natural fluor-apatites. *Journal of Luminescence* 69,
850 343–353. https://doi.org/10.1016/S0022-2313(96)00114-7
851
852 Rey C., Marsan O., Combes C., Drouet C., Grossin D., Sarda S. (2014) Characterization of
853 Calcium Phosphates Using Vibrational Spectroscopies. In: Ben-Nissan B. (eds) Advances in
854 Calcium Phosphate Biomaterials. Springer Series in Biomaterials Science and Engineering,
855 vol 2. Springer, Berlin, Heidelberg. https://doi.org/10.1007/978-3-642-53980-0_8
856
857 Suarez C.A., Machpherson G.L., González L.A., Grandstaff D.E. (2010) Heterogeneous rare
858 earth element (REE) patterns and concentrations in a fossil bone: Implications for the use of

REE in vertebrate taphonomy and fossilization history. *Geochimica and Cormochimica Acta* 74, 10, 2970-2988. https://doi.org/10.1016/j.gca.2010.02.023

Sun, S.-S. and McDonough, W.-s. (1989) Chemical and isotopic systematics of oceanic basalts: implications for mantle composition and processes. Geological Society, London, Special Publications 42, 313-345. https://doi.org/10.1144/GSL.SP.1989.042.01.19

Syassen K. (2008) Ruby under pressure, *High Pressure Research* 28:2, 75-126, DOI: 10.1080/08957950802235640

Waychunas, G.A. (2014) Luminescence Spectroscopy. *Reviews in Mineralogy and Geochemistry* 78, 175–217. https://doi.org/10.2138/rmg.2014.78.5

Waychunas, G.A. (2002) Apatite Luminescence. *Reviews in Mineralogy and Geochemistry* 48, 701–742. https://doi.org/10.2138/rmg.2002.48.19

Webster, J.D., Piccoli, P.M. (2015) Magmatic Apatite: A Powerful, Yet Deceptive, Mineral. *Elements* 11, 177–182. https://doi.org/10.2113/gselements.11.3.177

Wiens, R.C., Maurice, S., Robinson, S.H. *et al.* (2021) The SuperCam Instrument Suite on the NASA Mars 2020 Rover: Body Unit and Combined System Tests. *Space Science Reviews* 217**,** 4. https://doi.org/10.1007/s11214-020-00777-5

Figures Caption

Figure 1: Chondrite-normalized REE patterns from ICP-MS analysis of natural apatites (normalization factor from Sun and McDonough,1989).

Figure 2: XRD difractograms for the synthetic hydroxylapatites doped with europium at increasing concentration (see table 2 for measured concentration). Similar cristallinity was obtained for the other samples doped with other REE^{3+}.

Figure 3: Fourier Transform Infrared spectra for the synthetic hydroxylapatites doped with europium at increasing concentration (see table 2 for measured concentration). Similar cristallinity was obtained for the other samples doped with other REE^{3+}.

Figure 4: Representative continuous-wave Raman and luminescence spectra of synthetic hydroxylapatites doped with europium (a), samarium (b), dysprosium (c) and neodymium (d). All spectra are raw data, excitation at 532 nm except for neodymium (785 nm) and are acquired with the same acquisition time for each series. Note the strong background affecting the spectrum Sm2. R indicates a Raman peak.

Figure 5: Representative Raman spectra obtained on an hydroxylapatite doped with 23,936 ppm of samarium. The CW spectrum was obtained with the TR instrument by opening the gate for 450,000 ns (nearly pulse to pulse at 2 KHz) and including the laser pulse: the luminescence signal from samarium completely masks the Raman signal. The TR spectrum was obtained with the TR instrument by opening the gate for 5 ns including the laser pulse: the luminescence signal from samarium is completely rejected and the Raman signal is clearly visible.

Figure 6: Representative continuous-wave (green, ICCD gate of 450,000 ns including the laser pulse) and time-resolved (red, ICCD gate of 5 ns centered on the laser pulse) Raman spectra of some natural apatites. All spectra are raw data.

Figure 7: Time-resolved Raman and luminescence spectra obtained on the Durango apatite by using various combinations of delay and gates for the ICCD. From top to bottom: green is obtained with a long gate (450,000 ns) including the laser pulse, red is obtained with a short gate (5 ns) including the laser pulse, black is obtained with a long gate (450,000 ns) opened just after the laser pulse (10 ns), pale grey is obtained with a gate of 1,500 ns opened just after the laser pulse (5 ns), dark grey is obtained with long gate (450,000 ns) opened 1,500 ns after the laser pulse

Figure 8: Time-resolved luminescence spectra obtained on the Durango apatite by using a constant delay and increasing progressively the opening of the ICCD gate.

Figure 9: Diagrams showing the surface of the luminescence bands versus the doping element concentration for the 620 nm massif for europium (a) and the 600 nm massif for samarium (b). The grey inset depict the same diagram at low concentration (<3,000 ppm).

Figure 10: Result of the time-sweep experiment for Eu- and Sm-doped hydroxylapatites (see table 2 for measured concentration). The plots depict the normalized intensity of the 620 nm massif for Eu (a) and 600 nm massif for Sm (b) versus the delay of the ICCD gate. This figure illustrates the time decay of luminescence signal for Eu (a) and Sm (b). Lifetime is calculated as the slope of the line going through the experimental points.

Figure 11: Compilation of lifetime of luminescence for europium (a) and Samarium (b) versus the concentration in activator, europium (a) and samarium (b) respectively for the synthetic REE-doped and natural apatites.

Table 1: Nd, Sm, Eu and Dy composition of the synthetic hydroxyapatite samples measured by ICP-MS. (µg/g = ppm; < L.D below limit of detection).

Sample reference	**Nd** µg/g	**Sm** µg/g	**Eu** µg/g	**Dy** µg/g	**CaO** wt%	**P_2O_5** wt%
Eu 1	0	0	42	0	53.02	39.01
Eu 2	0	0	128	0	53.06	38.92
Eu 3	0	< L.D.	270	0	53.34	39.36
Eu 4	0	0	1 317	0	52.80	38.63
Eu 5	0	0	2 562	0	52.33	37.87
Eu 6	0	0	25 601	0	50.02	37.36
Sm 1	0	24	5	0	52.77	39.17
Sm 2	0	115	5	0	52.06	37.89
Sm 3	0	240	1	0	53.31	39.82
Sm 4	0	1 251	0	0	52.35	38.47
Sm 5	0	2 450	0	0	52.37	38.31
Sm 6	0	23 936	1	1	50.06	37.13
Nd 1	24	4	< L.D.	0	52.91	38.83
Nd 2	115	1	< L.D.	0	52.46	38.14
Nd 3	228	0	< L.D.	1	52.81	38.84
Nd 4	1 185	3	2	2	53.16	39.03
Nd 5	2 475	0	0	5	52.57	38.45
Nd 6	24 832	2	1	50	50.59	39.91
Dy 4	4	< L.D.	0	1 358	51.89	38.16

Table 2: Major elements (oxide wt%) and REE composition (µg/g or ppm) of the natural apatite samples measured by ICP-MS (< L.D below limit of detection).

	Tyrol	**Imilchil**	**Renfrew**	**Slyudyanka**	**Durango**
Location	Tyrol – Austria	Imilchil – Morocco	Renfrew, Ontario – USA	Lake Baikal, Russia	Durango – Mexico
Type	fluorapatite	fluorapatite	fluorapatite	unknown	fluorapatite
Form	polycristal	polycristal	polycristal	polycristal	monocristal
Color	dark green	light green – yellow	light green	light blue	yellow
CaO	53.23	53.35	54.11	54.34	53.58
P_2O_5	39.83	41.47	40.72	39.92	40.68
MnO	< L.D.	0.02	0.11	< L.D.	< L.D.
Sc	2	1	1	< L.D.	1
Y	297	1418	1643	46	452
La	992	2590	741	75	3166
Ce	2290	4138	2058	136	4030
Pr	276	438	297	14	332
Nd	994	1794	1264	49	1045
Sm	147	407	302	9	131
Eu	13	41	27	2	16
Gd	94	397	308	8	112
Tb	11	54	55	1	13
Dy	56	286	353	8	72
Ho	10	52	74	2	14
Er	23	119	197	4	37
Tm	3	13	27	1	5
Yb	15	61	141	3	26
Lu	2	6	17	0	4

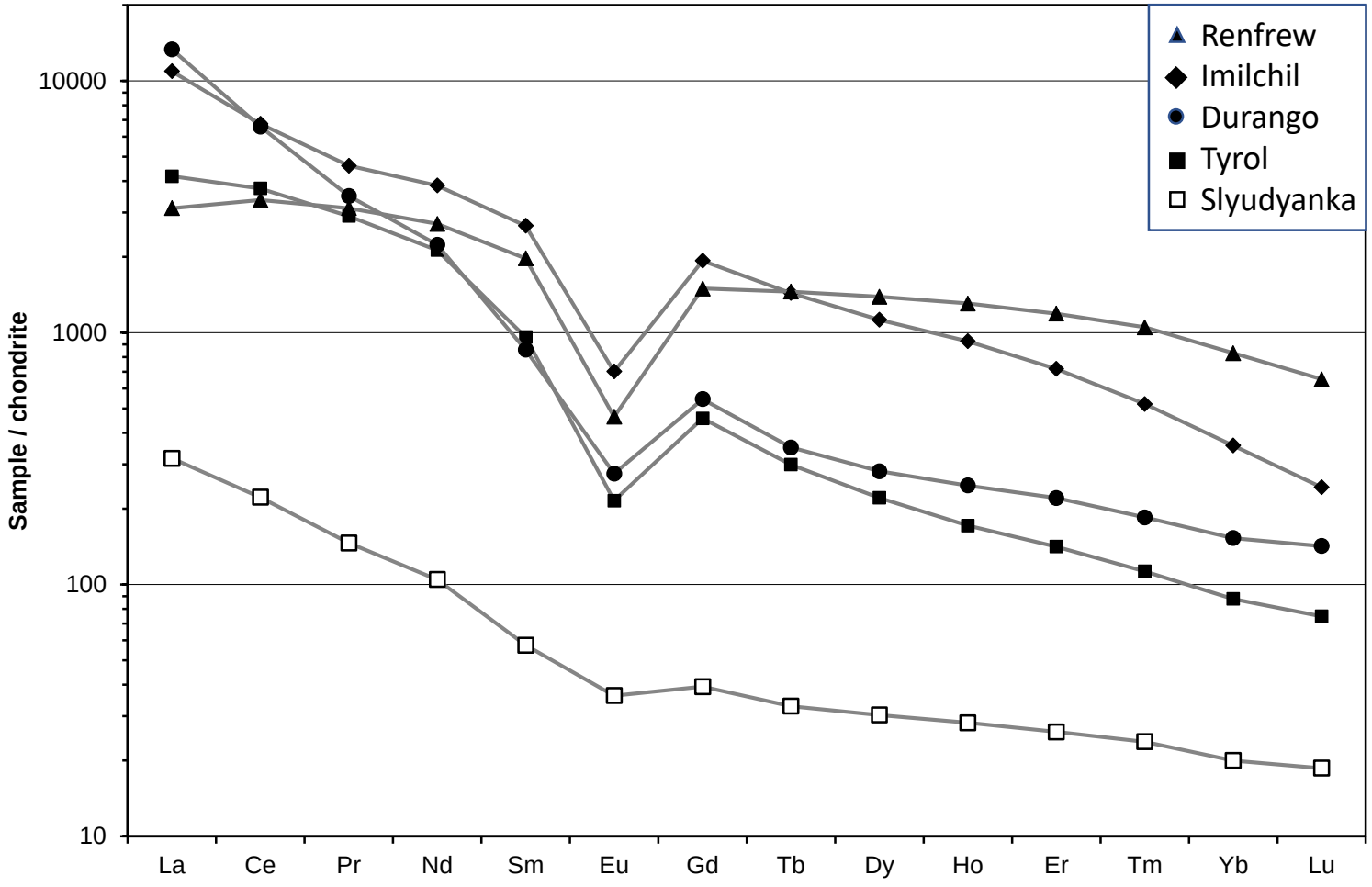
Renfrew
Imilchil
Durango
Tyrol
Slyudyanka
Sample / chondrite
10000
1000
100
10
La
Ce
Pr
Nd
Sm
Eu
Gd
Tb
Dy
Ho
Er
Tm
Yb
Lu

Figure 1

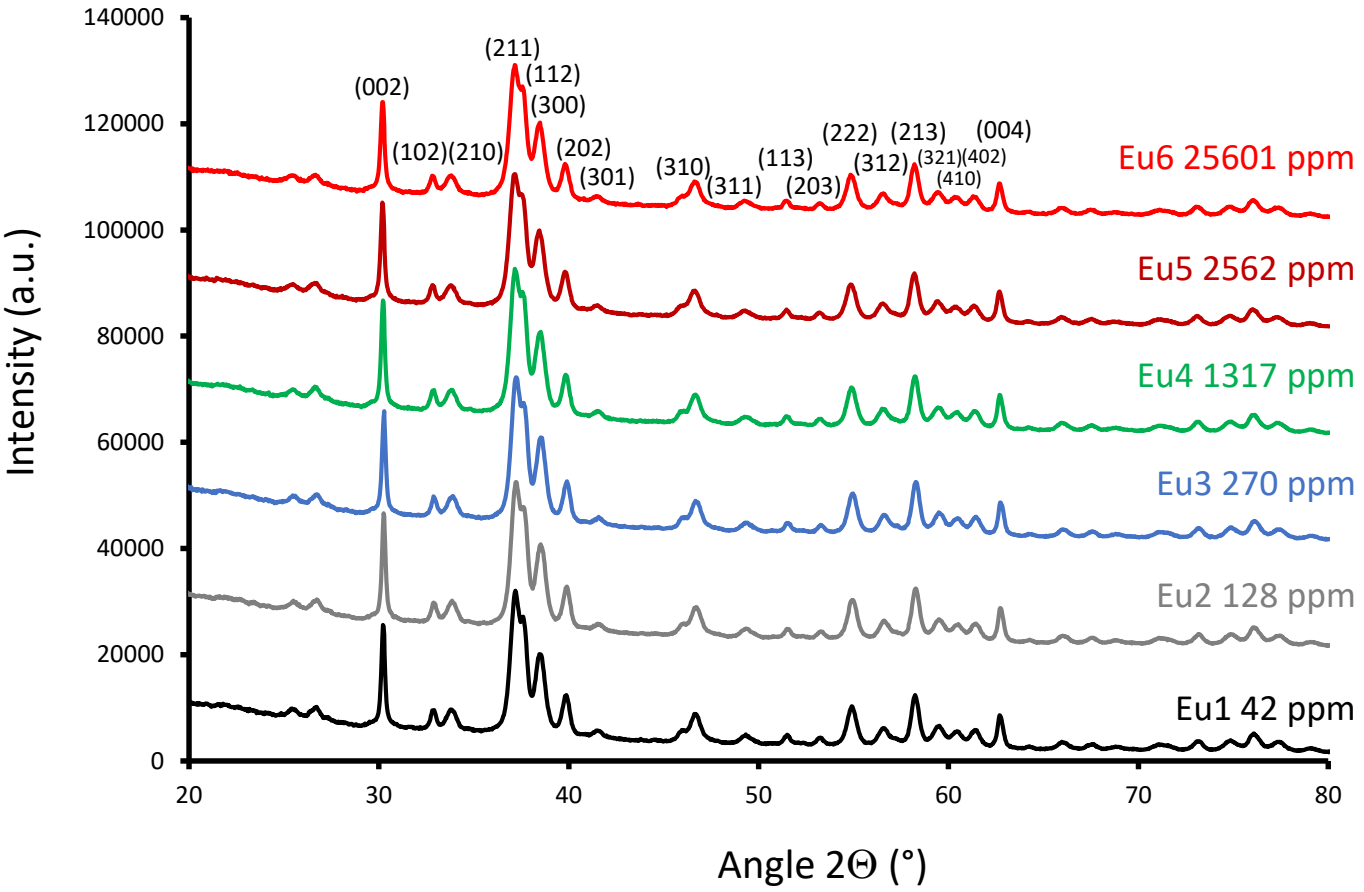
Intensity (a.u.)
140000
120000
100000
80000
60000
40000
20000
0
20
30
40
50
60
70
80
Angle 2Θ (°)
(002)
(102)(210)
(211)
(112)
(300)
(202)
(301)
(310)
(311)
(113)
(203)
(222)
(312)
(213)
(321)(402)
(410)
(004)
Eu6 25601 ppm
Eu5 2562 ppm
Eu4 1317 ppm
Eu3 270 ppm
Eu2 128 ppm
Eu1 42 ppm

Figure 2

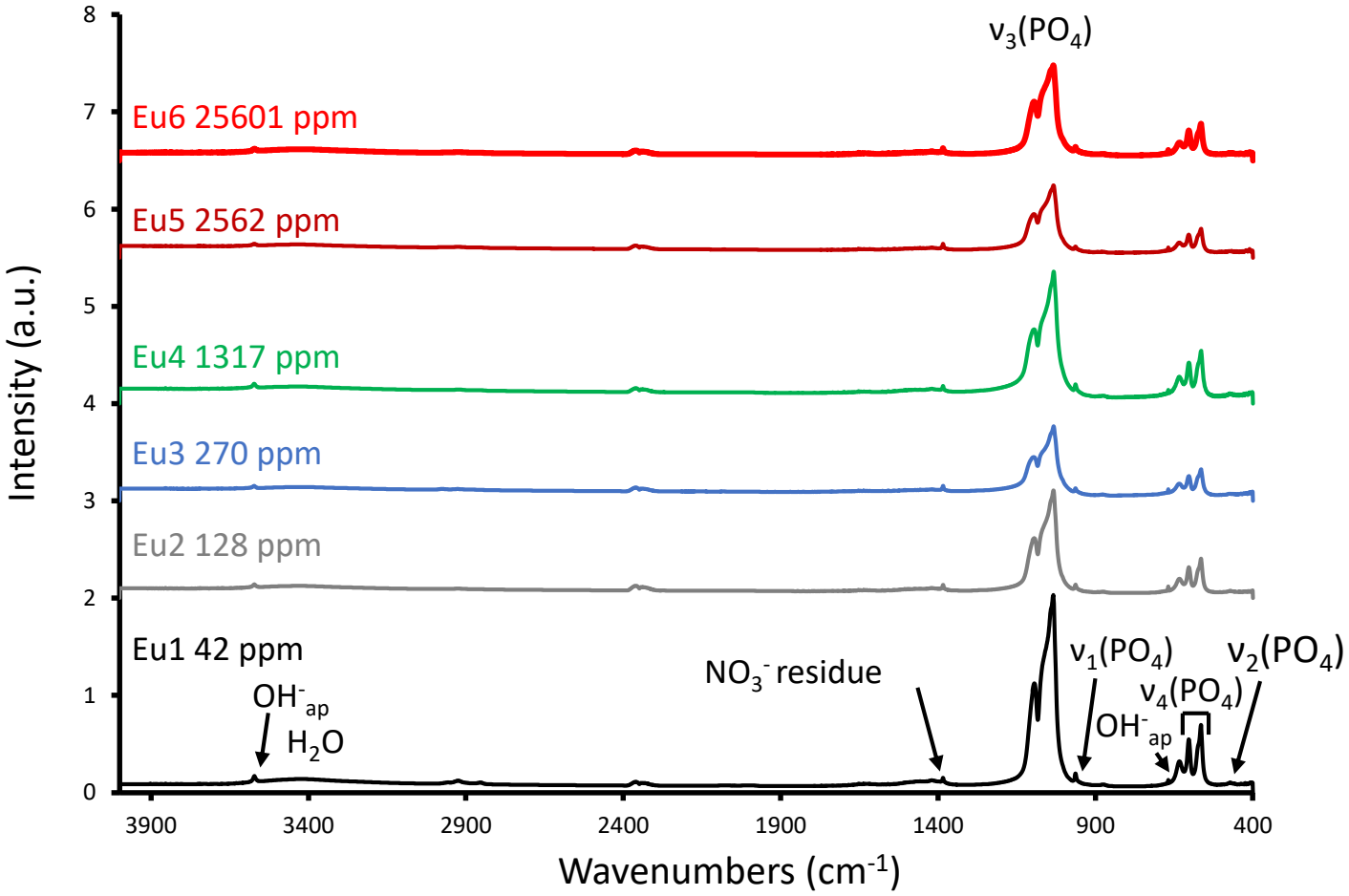
Intensity (a.u.)
Wavenumbers (cm-1)
Eu6 25601 ppm
Eu5 2562 ppm
Eu4 1317 ppm
Eu3 270 ppm
Eu2 128 ppm
Eu1 42 ppm
ν3(PO4)
ν1(PO4)
ν2(PO4)
ν4(PO4)
NO3- residue
OH-ap
H2O
OH-ap
0
1
2
3
4
5
6
7
8
3900
3400
2900
2400
1900
1400
900
400

Figure 3

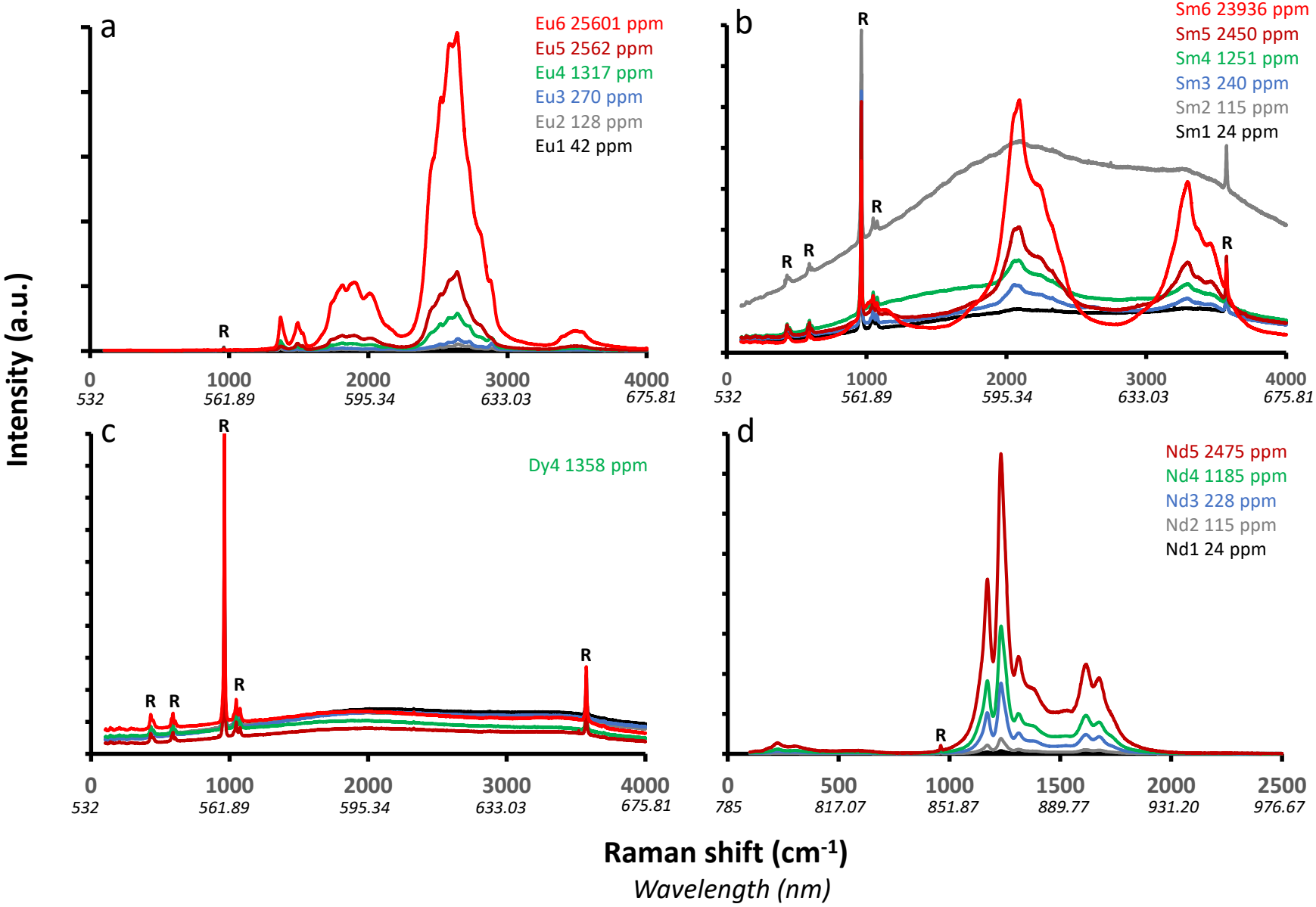
a
Eu6 25601 ppm
Eu5 2562 ppm
Eu4 1317 ppm
Eu3 270 ppm
Eu2 128 ppm
Eu1 42 ppm
R
0
1000
2000
3000
4000
532
561.89
595.34
633.03
675.81
b
Sm6 23936 ppm
Sm5 2450 ppm
Sm4 1251 ppm
Sm3 240 ppm
Sm2 115 ppm
Sm1 24 ppm
R
R
R
R
R
0
1000
2000
3000
4000
532
561.89
595.34
633.03
675.81
c
Dy4 1358 ppm
R
R
R
R
R
0
1000
2000
3000
4000
532
561.89
595.34
633.03
675.81
d
Nd5 2475 ppm
Nd4 1185 ppm
Nd3 228 ppm
Nd2 115 ppm
Nd1 24 ppm
R
0
500
1000
1500
2000
2500
785
817.07
851.87
889.77
931.20
976.67
Intensity (a.u.)
Raman shift (cm-1)
Wavelength (nm)

Figure 4

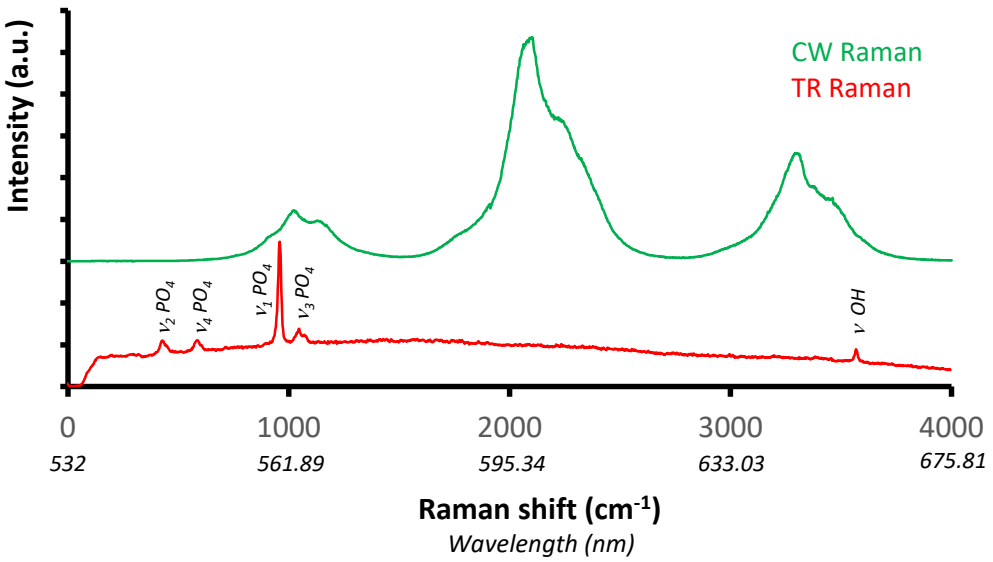
Intensity (a.u.)
CW Raman
TR Raman
ν2 PO4
ν4 PO4
ν1 PO4
ν3 PO4
ν OH
0
1000
2000
3000
4000
532
561.89
595.34
633.03
675.81
Raman shift (cm-1)
Wavelength (nm)

Figure 5

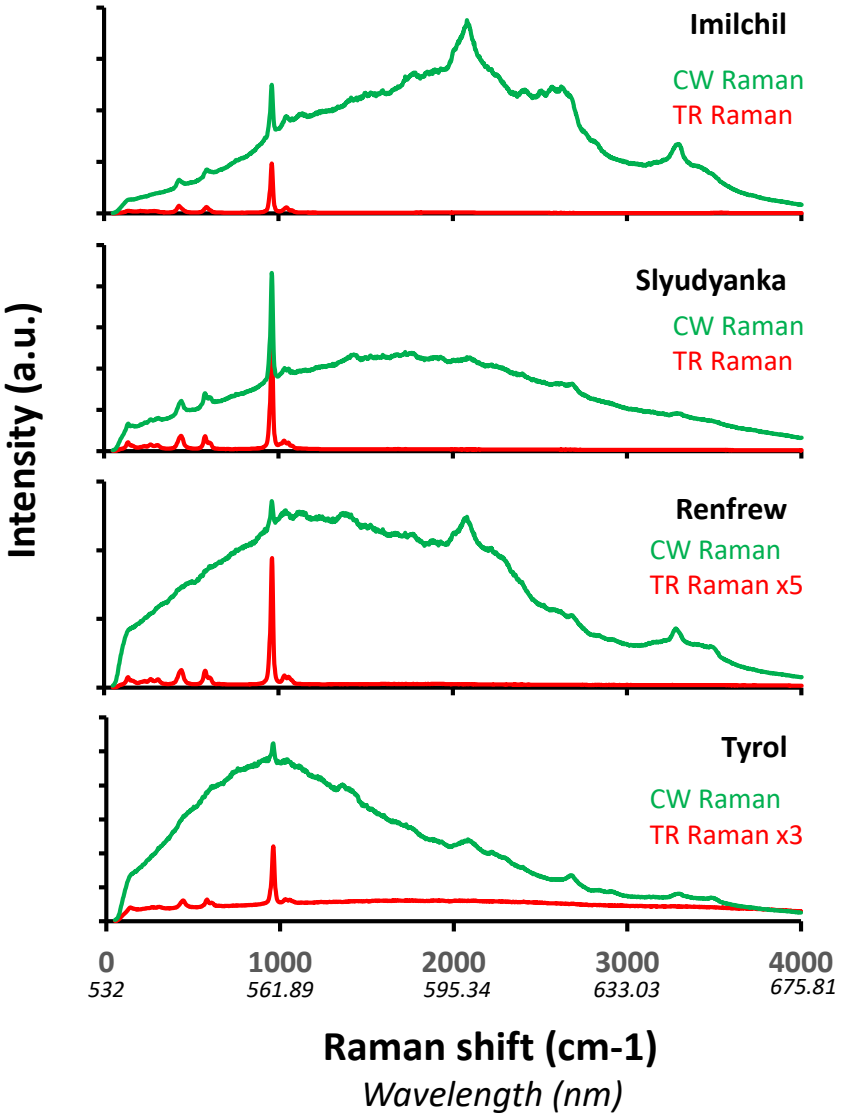
Imilchil
CW Raman
TR Raman
Slyudyanka
CW Raman
TR Raman
Renfrew
CW Raman
TR Raman x5
Tyrol
CW Raman
TR Raman x3
Intensity (a.u.)
0
532
1000
561.89
2000
595.34
3000
633.03
4000
675.81
Raman shift (cm-1)
Wavelength (nm)

Figure 6

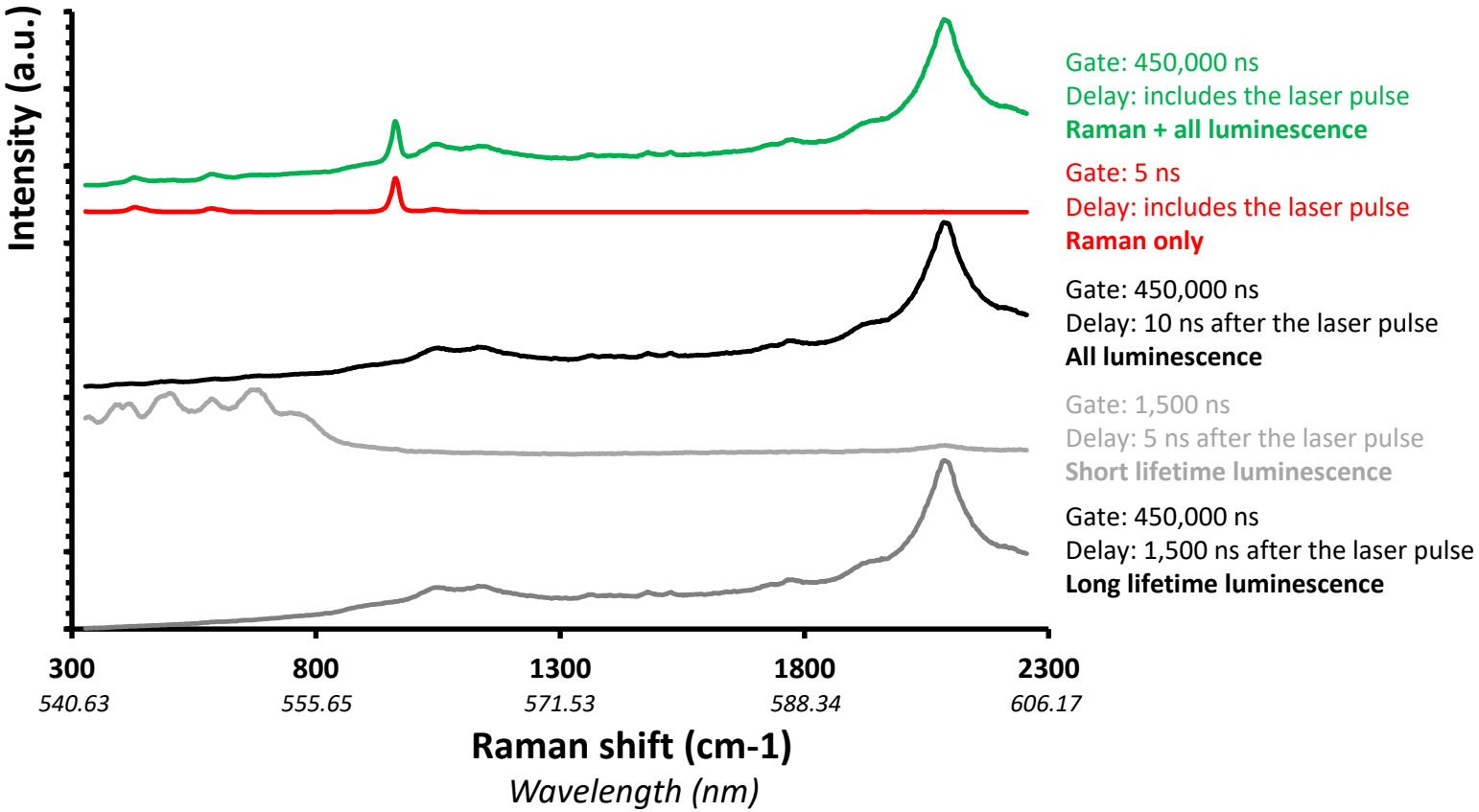
Intensity (a.u.)
300
800
1300
1800
2300
540.63
555.65
571.53
588.34
606.17
Raman shift (cm-1)
Wavelength (nm)
Gate: 450,000 ns
Delay: includes the laser pulse
Raman + all luminescence
Gate: 5 ns
Delay: includes the laser pulse
Raman only
Gate: 450,000 ns
Delay: 10 ns after the laser pulse
All luminescence
Gate: 1,500 ns
Delay: 5 ns after the laser pulse
Short lifetime luminescence
Gate: 450,000 ns
Delay: 1,500 ns after the laser pulse
Long lifetime luminescence

Figure 7

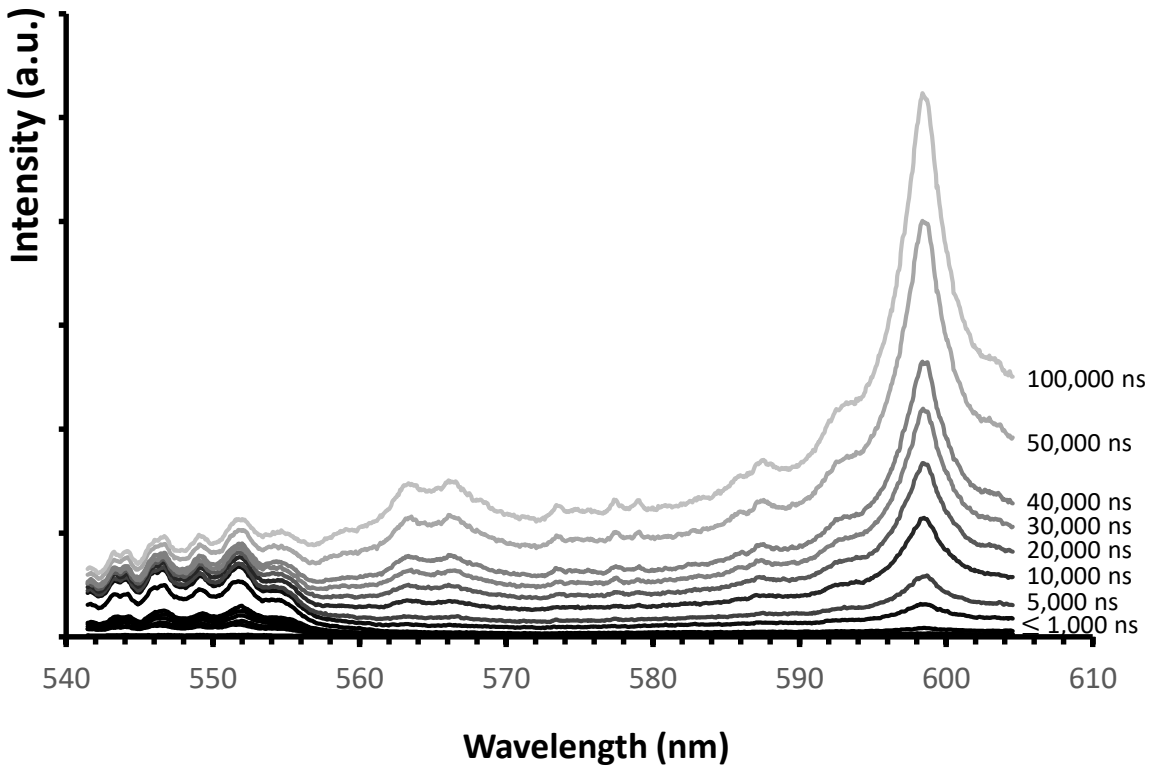
Intensity (a.u.)
100,000 ns
50,000 ns
40,000 ns
30,000 ns
20,000 ns
10,000 ns
5,000 ns
< 1,000 ns
540
550
560
570
580
590
600
610
Wavelength (nm)

Figure 8

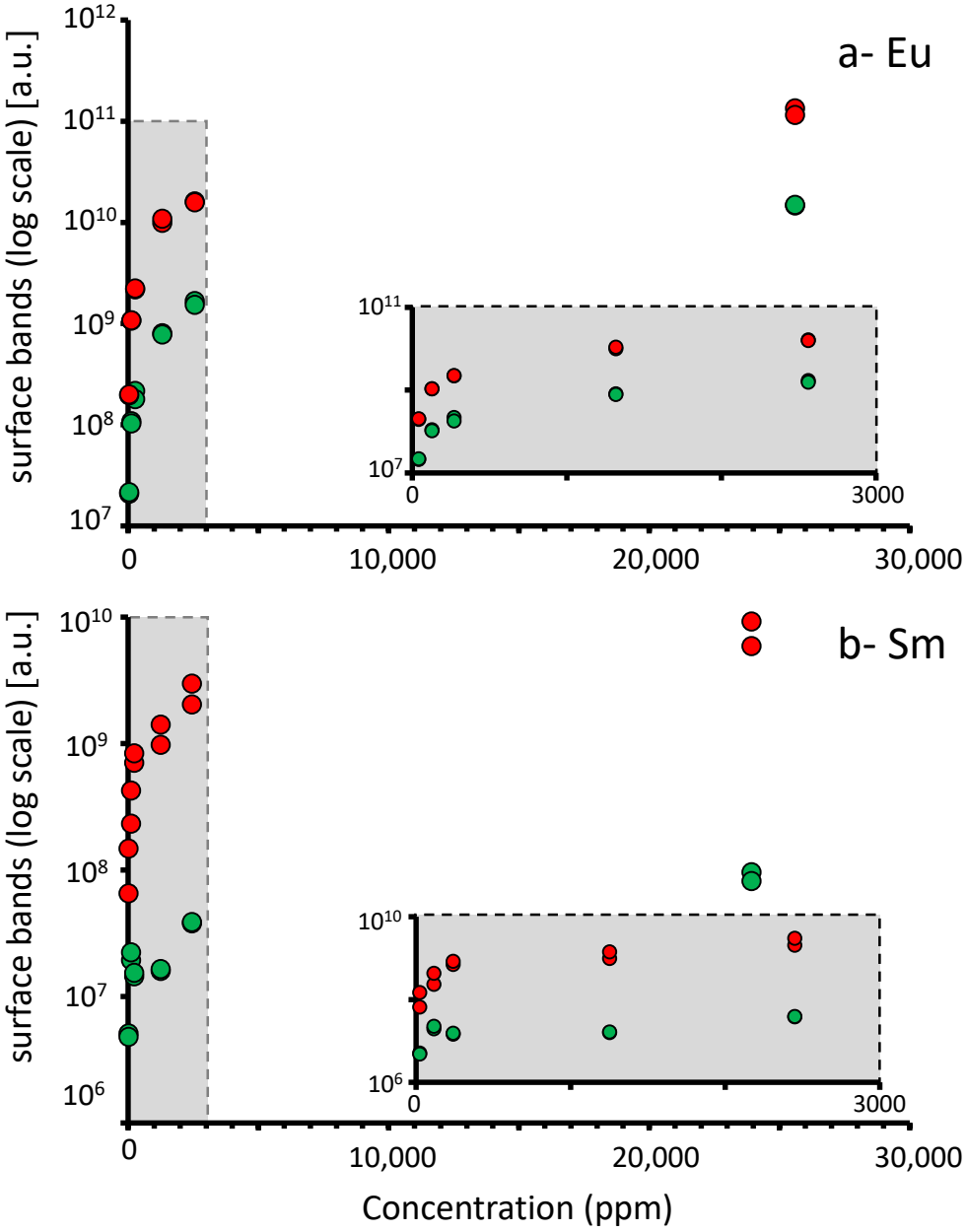
a- Eu
b- Sm
surface bands (log scale) [a.u.]
Concentration (ppm)
0
10,000
20,000
30,000
3000

Figure 9

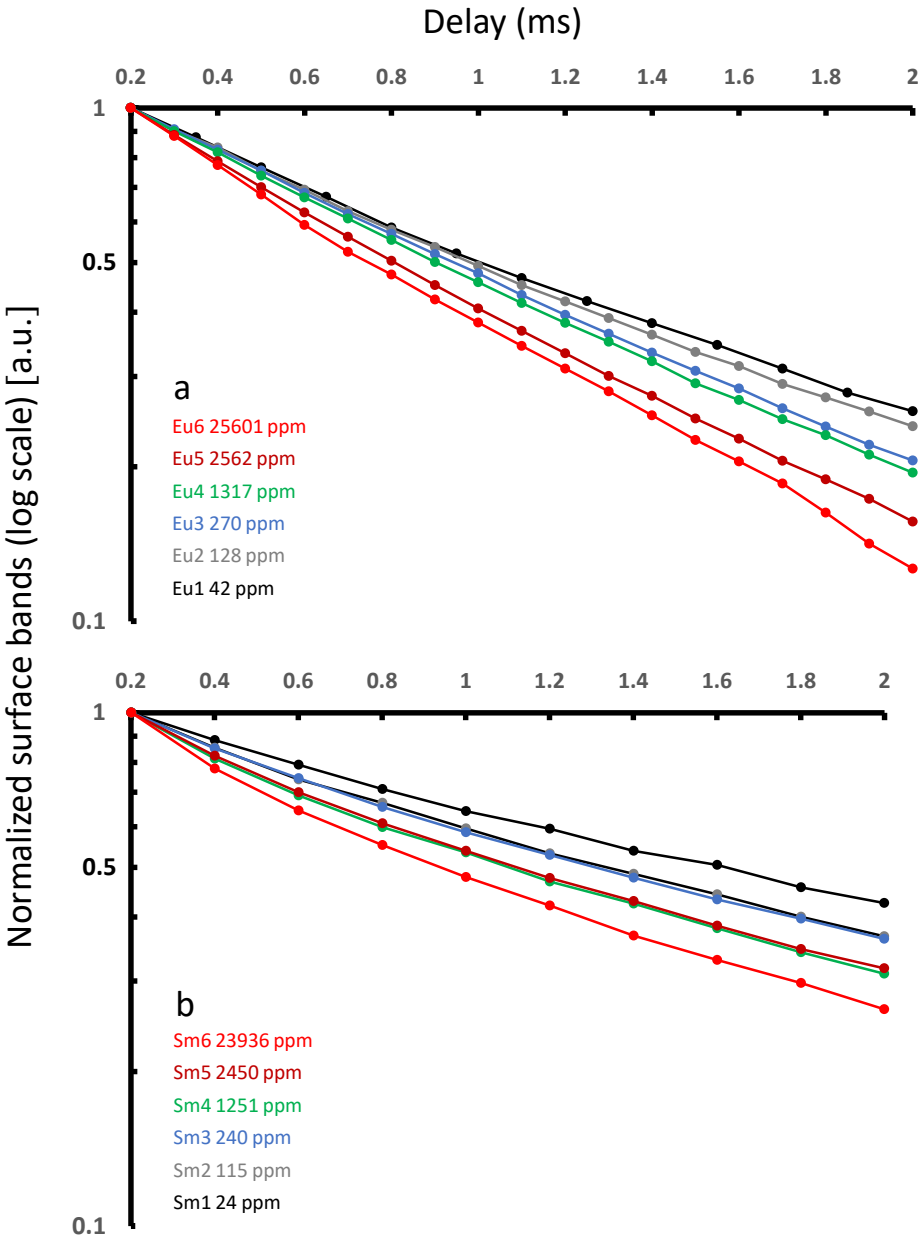
Delay (ms)
0.2
0.4
0.6
0.8
1
1.2
1.4
1.6
1.8
2
Normalized surface bands (log scale) [a.u.]
1
0.5
0.1
a
Eu6 25601 ppm
Eu5 2562 ppm
Eu4 1317 ppm
Eu3 270 ppm
Eu2 128 ppm
Eu1 42 ppm
b
Sm6 23936 ppm
Sm5 2450 ppm
Sm4 1251 ppm
Sm3 240 ppm
Sm2 115 ppm
Sm1 24 ppm

Figure 10

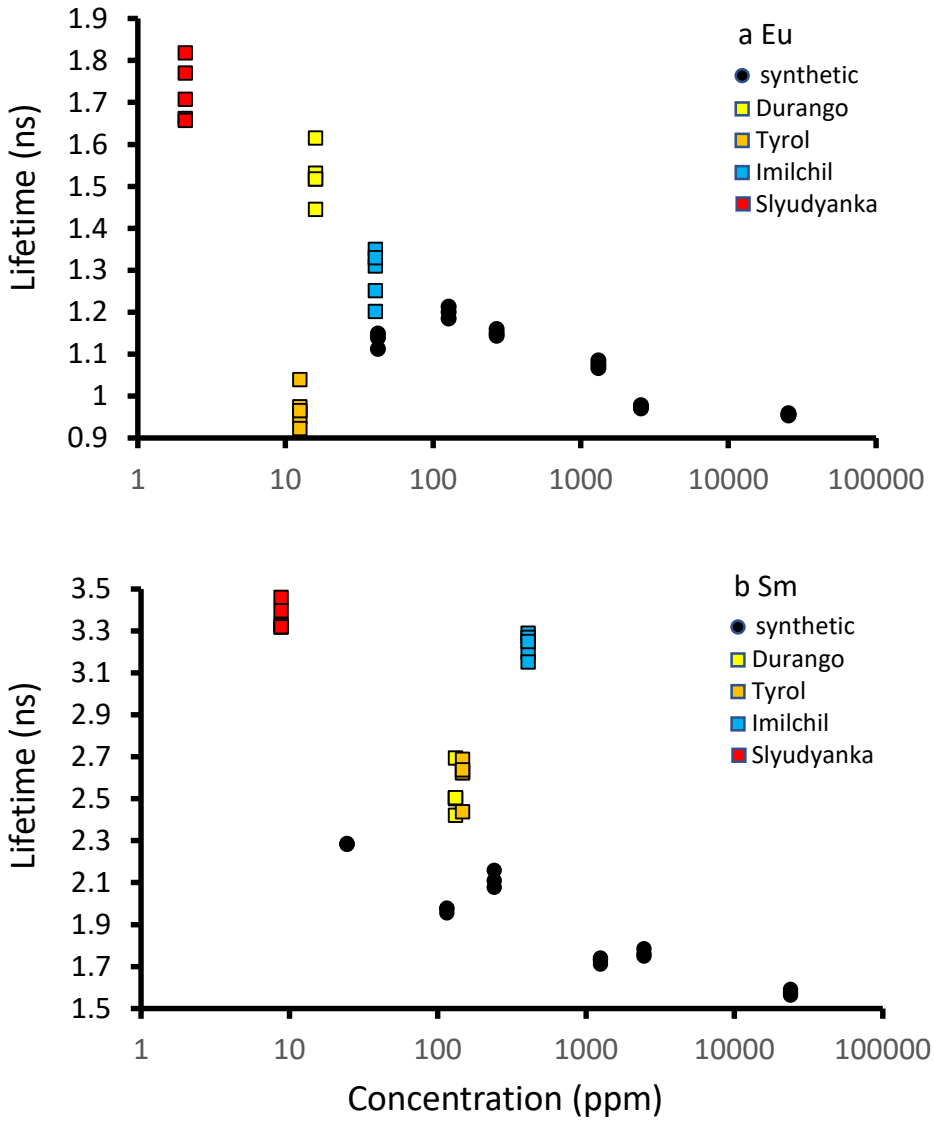
a Eu
synthetic
Durango
Tyrol
Imilchil
Slyudyanka
Lifetime (ns)
1.9
1.8
1.7
1.6
1.5
1.4
1.3
1.2
1.1
1
0.9
1
10
100
1000
10000
100000
b Sm
synthetic
Durango
Tyrol
Imilchil
Slyudyanka
Lifetime (ns)
3.5
3.3
3.1
2.9
2.7
2.5
2.3
2.1
1.9
1.7
1.5
1
10
100
1000
10000
100000
Concentration (ppm)

Figure 11